Title
High-Resolution Imaging of Unstained Polymer Materials

Journal
ACS Applied Polymer Materials, 3(6)

ISSN
2637-6105

Authors
Jiang, Xi
Balsara, Nitash P

Publication Date
2021-06-11

DOI
10.1021/acsapm.1c00217

Peer reviewed

High-Resolution Imaging of Unstained Polymer Materials

Xi Jiang [1], Nitash P. Balsara[1,2]**

1. Materials Sciences Division, Lawrence Berkeley National Laboratory, Berkeley, CA 94720, USA

2. Department of Chemical and Biomolecular Engineering, University of California, Berkeley, CA 94720, USA

*Corresponding author: xijiang@lbl.gov; nbalsara@berkeley.edu

ORCID:

Xi Jiang, https://orcid.org/0000-0002-9589-7513

Nitash P. Balsara, https://orcid.org/0000-0002-0106-5565

Keywords: transmission electron microscopy, four-dimensional scanning transmission electron microscopy, cryogenic, low-dose imaging, unstained

Abstract

Electron microscopy has played an important role in polymer characterization. Traditionally, electron diffraction is used to study crystalline polymers while transmission electron microscopy is used to study microphase separation in stained block copolymers and other multiphase systems. We describe developments that eliminate the barrier between these two approaches – it is now possible to image polymer crystals with atomic resolution. The focus of this review is on high-resolution imaging (30 Å and smaller) of unstained polymers. Recent advances in hardware allow for capturing numerous (as many as 10^5) low-dose images from an unperturbed specimen; beam damage is a significant barrier to high-resolution electron microscopy of polymers. Machine-learning-based software is then used to sort and average the images to retrieve pristine structural information from a collection of noisy images. Acknowledging the heterogeneity in polymer samples prior to averaging is essential. Molecular conformations in a wide range of amphiphilic block copolymers, polymerized ionic liquids and conjugated polymers, can be gleaned from two-dimensional projections (2D), three-dimensional (3D) tomograms, and four-dimensional (4D) scanning transmission electron microscopy (STEM) datasets where 2D diffraction patterns are taken as a function of position. Some methods such as phase contrast STEM have been used to image closely related materials such as metal-organic frameworks but not polymers. With improvements in hardware and software, such methods may soon be applied to polymers. Our goal is to provide a comprehensive understanding of the strategies toward the high-resolution imaging of radiation sensitive polymer materials at different length scales.

1. Introduction

The morphology of polymer materials depends on chemical structure of the monomer, the presence of side-chains in the monomer and the nature of the bonds that connect the monomers. Determining the location of the atoms that make up a polymer chain is important as they govern the properties of polymer materials; however, we seldom have direct knowledge of their location. The main purpose of this review is to summarize recent advances in the field of electron microscopy that have the potential to significantly improve the resolution of images obtained from polymer samples.

In conventional synthetic polymers, chain molecules exist in two states: crystalline and amorphous. Homopolymers in the crystalline state adopt folded two-dimensional (2D) lamellar crystals that are arranged in three-dimensional (3D) spherulites.[1] In block copolymers comprising two or more blocks of chemically distinct repeating units, the morphologies obtained are more complex due to the additional factors related to thermodynamic interactions between different monomers.[2]. Spontaneous microphase separation of the blocks results in the formation of 2D and 3D nanostructures, such as lamellae, cylinders, gyroid and helices, on the 2 to 100 nanometer length scales.[3-12] The chains in each of the microphases can be either crystalline or amorphous. A fundamental challenge in polymer science is to design nanoarchitectures assembled from polymers with precisely controlled structures and properties. Information of chain conformations is therefore desired at the atomic length scale.

Ernst Ruska developed the first electron microscope (EM) which enabled both direct imaging in position space and electron diffraction in reciprocal space.[13] The resolution was unprecedented as the wavelength of electron beams (typically 0.002 nm) is much shorter than X-rays (typically 0.15 nm). In a landmark study in 1938, Storks demonstrated that electron diffraction could be

used to characterize crystalline polymer materials.[14] In 1950s, Keller and coworkers studied the folded chain configurations and lattice structure of polyethylene (PE) single crystals using transmission electron microscopy (TEM) imaging and diffraction.[15-18] Since then, electron diffraction has led to the determination of crystal structure of numerous other homopolymers such as polyethylene oxide (PEO), and polypropylene (PP), and block copolymers such as polyethylene oxide-*b*-polystyrene (PEO-*b*-PS).[19-34]

It is challenging to obtain structural information of polymers due to their limited stability under electron beam radiation. Keller and coworkers realized the importance of radiation damage, noting that the diffraction signatures of crystalline order in PE crystals disappeared as the electron dose increased.[21, 35] In 1971, Glaeser studied radiation damage in crystalline biological materials.[36] Included in this study were measurements of the intensities of the Bragg reflections in the electron diffraction patterns that led to a quantitative understanding of the relationship between radiation damage and spatial resolution. Since then, numerous papers have been written on the subject of radiation damage in biological materials.[37-38] The Glaeser method has been also widely used to study radiation damage in polymer materials.[26, 37, 39-45] The extent of radiation damage in both crystalline and amorphous polymer, based on the work of Keller and coworkers, was summarized by Grubb.[46] A fraction of the incident beam of high energy electrons is scattered as it interacts with the polymer specimen (which is usually thin for transmission electron microscopy (TEM)). While the scattered electrons can be the result of inelastic or elastic scattering events, the inelastic-to-elastic scattering ratio is governed by atomic number Z (experimentally scales as 20/Z).[47] In the polymer materials comprising light elements, the scattered electrons are mainly inelastic and it is these electrons that are primarily responsible for radiation damage; they induce plasmon excitation and subsequent ionization.[47] Signatures of the

early stage of radiation damage, namely loss of diffraction patterns, give way to mass loss and the appearance of bubbles due to beam-induced chemical reactions as the accumulated electron dose increases. An example of such a reaction is formation of hydrogen gas in hydrocarbon polymers. In order to prevent radiation damage in typical aliphatic polymers, the accumulated electron dose deposited on the field of view, where an image is acquired, must be between 5 to 30 $e/Å^2$.[22-23, 48-51] Aromatic polymers show higher tolerance of electron dose relative to aliphatic polymers due to the delocalization of electrons. [37, 52-54] In addition, the tolerance of radiation damage of aromatic polymers can be increased by using a graphene supporting film [55] or adding an antioxidant.[45] More details about the dependence of radiation damage on temperature, dose rate, acceleration voltage and the specificity of damage to different polymers can be found elsewhere.[56] Nevertheless, some form of beam damage must be endured if larger doses are used in an attempt to increase signal-to-noise.

Electron diffraction has historically been the standard approach for studying the structure of crystalline polymers. In the same field of view, scattered waves from a large number of unit cells in that field interfere constructively to give strong diffraction patterns which can be interpreted in terms of the underlying unit cell; staining is unnecessary. In contrast, the microphase separated structures in most of block copolymers cannot be directly observed by bright field TEM due to the lack of contrast in amorphous regions. Andrews and coworkers first demonstrated the staining of a rubbery phase in a polymer using osmium tetroxide in 1964.[57-58] This protocol was further developed by Kato to image the thin sections of acrylonitrile-butadiene-styrene (ABS) resin where the amorphous unsaturated polybutadiene domains were positively stained by osmium tetroxide.[59-60] Other staining agents, such as ruthenium tetroxide, iodine, and lead acetate, were used to stain the other targeted polymers. Ruthenium tetroxide has

been widely used to stain polymers that contain ether, alcohol, aromatic, and amine functional groups.[61] Iodine is used to stain the pyridine rings, through the formation of a pyridinium salt.[62-63] Lead acetate can increase the electron density of ion-containing hydrophilic blocks after ion exchange.[64-65] Most synthetic crystalline polymers are, strictly speaking, semicrystalline. In other words, the crystalline unit cells coexist with amorphous domains. These amorphous domains can be selectively stained by osmium tetroxide and ruthenium tetroxide in polyolefins and polyamides to reveal a more complete description of 2D and 3D morphologies.[66-70] The direct staining of the objects of interest is referred to as positive staining. Negative staining agents such as uranyl acetate or uranyl formate are used to increase electron scattering from the background around the objects of interest, thereby enhancing the signal-to-noise ratio of the image. This method has been widely used to examine the morphology of self-assembled structures in solution – the structures are deposited on a substrate, dried, and collapsed.[71-72]

Staining has become a standard protocol for TEM imaging of polymers. In addition to increasing contrast between phases comprising light elements, staining agents, which invariably contain heavy elements, reduce electron beam damage. However, the introduction of compounds that are not in the material of interest and the processes by which they are introduced can lead to the introduction of artifacts. Ruthenium tetroxide, for example, is often introduced by placing polymers in the vicinity of aqueous solutions. Water vapor can swell domains that are hydrophilic, *e.g.*, poly(ethylene oxide). Care must be taken to ensure that the staining agent does not aggregate in one part of the sample (*e.g.*, the surface). If the local concentration of the staining agent becomes high enough, it could diffuse into domains that are not the target of the staining process.[68, 73] Negative staining can produce artifacts such as aggregation, flattening and

stacking of structures.[74-75] *What is more important, however, is the loss of high-resolution structural information and the absence of the natural state in the stained specimens.*

The two major problems, radiation damage and low contrast, must be addressed when the high-resolution images of polymers are desired. Cryogenic transmission electron microscopy (cryo-TEM), which was initially developed by the structural biology community, is a powerful tool to retrieve the high-resolution information of radiation sensitive materials.[76-78] In this approach, many (of order 10^5) images of the sample with low signal-to-noise ratio (SNR) are obtained at liquid nitrogen temperatures to reduce beam damage. Sophisticated machine-learning-based algorithms are used to align, filter, and average the images to obtain a high-resolution image that represents the specimen in its natural state.[79-80] More recently, the resolution of cryo-TEM was significantly improved by the introduction of direct electron detectors and novel image processing algorithms.[81-82] The high detective quantum efficiency (DQE) of direct electron detectors enables fast and automated image recording that give dose-fractionated frames in a movie which allows for the correction of beam-induced movement of monomers (and atoms) in the specimen.[83] The nature of the image contrast in a bright field TEM micrograph can be described by the "weak-phase object" approximation when a thin specimen comprising soft materials is imaged. In this approximation, the relationship between the electron density contrast in a specimen and the image is described by a linear transfer function. The contrast transfer function (CTF) is introduced to relate the electron density variation in the specimen to the image in Fourier space. This function depends on spatial frequency, *s*, as shown in Eq 1.

$$CTF(s) = \sin\left\{2\pi\left[\frac{Cs}{4}\lambda^3 s^4 - \frac{\Delta Z}{2}\lambda s^2\right] + \varphi\right\} \qquad \text{(Eq 1)}$$

The first term in the square brackets accounts for spherical aberration of the microscope and *Cs* is an instrument-related constant, while the second term accounts for defocus and ΔZ represents the defocus value. λ is the wavelength of incident electrons. The last term φ represents the additional phase shift induced by phase plate. More details can be found in Chapter 3 and 4 in ref 47 and ref 84. When a micrograph is obtained using cryo-TEM without aberration correction, an appropriate amount of defocus, ΔZ, is applied to increase contrast and change the CTF to retrieve phase information.[84-85] Images of nanotubes, nanoparticles and vesicles can be misinterpreted due to the presence of Fresnel fringes that arise due to the applied defocus.[86] However, low spatial frequency signals can be recovered without applying defocus. A phase plate can be introduced at back focal plane of the objective lens to introduce a phase shift, φ,, ideally a $\pi/2$ phase shift, between the incident and scattered electrons. Either a Zernike phase plate or a Volta phase plate can be used.[87] Zernike phase plate has been used to observe the unstained polystyrene-*b*-polyisoprene block copolymer samples. The image obtained from the unstained sample exhibited similar resolution as that obtained from the OsO_4 stained sample.[88] The Volta phase plate operates due to beam-induced electrostatic charging of the surface of a continuous thin carbon film at high temperature (about 200°C). It boosted phase contrast in images of biological materials and carbon nanotubes.[89-94] By improving contrast and SNR, these approaches have the potential to improve our interpretation of structures in polymer materials which, like biological systems, are radiation-sensitive weak phase objects. A laser phase plate for in-focus phase contrast TEM, where the phase shift is controlled by a high-intensity continuous-wave laser beam, has been demonstrated to successfully provide a more stable and tunable phase shift by eliminating electrostatic charging and unwanted electron scattering.[95-96]

2D projections of a thin polymer specimen sometimes don't contain enough information to determine the 3D structure unambiguously. For example, considerable effort was necessary determine the 3D structure of the gyroid phase in block copolymers from 2D projections that often resembled "wagon-wheels".[11-12, 97-98] Cylinders oriented in the plane of the specimen are difficult to distinguish from lamellae with normals oriented in the specimen plane. [99]

There are three established approaches for 3D reconstruction:[109]

(1) The first method is electron tomography (ET). 2-D projections of the titled specimen are acquired at different tilt angles. The projections are aligned to a reference projection using fiducial markers or patches in the images that contain trackable features. Fourier transforms of projections are aligned to a central transform and the composite 3D Fourier transform is back projected to position space to obtain a 3D reconstruction of the specimen.[100] Different algorithms have been developed for the 3D tomographic reconstruction including weighted back projection, algebraic reconstruction, and iterative reconstruction.[101] ET has been used to characterize microphase separation under different imaging modes such as cryogenic electron tomography (Cryo-ET) and STEM electron tomography (STEM-ET). These approaches have been summarized by Jinnai *et al*.,[102] Nudelman and Patterson *et al*.,[103-104] , Bals *et al*.[105], Midgley and Weyland.[106]

(2) The second method is electron crystallography when atomic resolution imaging of a thin crystalline specimen is desired. It was developed initially by Henderson and Unwin,[107] to reconstruct the 3D structure of vitrified crystalline protein membranes by cryo-TEM, based on the DeRosier and Klug's principle.[108] The method comprises either aligning the Bragg reflections in electron diffraction patterns or images obtained from tilted specimens. More details

can be found in ref 47. This method has enabled atomic resolution of protein crystals and helices in microtubules.[109-111]

(3) The third method is single particle analysis (SPA). Multiple 2D projections are acquired from vitrified specimens comprising identical objects with random orientations (e.g. virus or proteins in vitreous ice). The location of each object in images is first identified. Then small segments of the image that contain one object are sorted into different classes according to the orientations of object and averaged using sophisticated algorithms.[112-113] The averaged images in each class are then back projected onto a 3D electron density map for further refinement of structure. Single particle analysis has been used to characterize polymer materials. The analysis has enabled identifying the heterogeneity in specimens (different classes), and resolving structures from the nanometer to Angstrom length scales, using 2-D projections[79-80, 114-116] and 3D reconstructions.[117-119]

It should be obvious that applying modern electron microscopy imaging techniques with the goal of obtaining atomic scale images requires working with unstained samples. In this review, we focus on the recent progress on structures formed by unstained polymers on different length-scales. The characteristics of the specific systems covered in this review are listed in Table 1, and sorted by resolution. The first two columns show the materials and the structures formed by these materials. This is followed by a listing of imaging and processing methods, imaging conditions, and resolution for each material. Table 1 also shows structural information retrieved from processed or reconstructed images.

We use the materials in Table 1 to answer three questions: (1) How can we accurately resolve the structures in the unstained polymers? (2) What information can we obtain from the

images at different length scales? (3) What issues need to be addressed to push the resolution of EM imaging of unstained polymers?

2. Self-assembled polymer nanostructures in solution

High-resolution temporal and spatial information obtained during the formation of polymer nanostructures is crucial for understanding the microphase separation mechanisms and the interactions between solvent molecules and polymer chains. Beginning with the pioneering work of Talmon et al.,[120] cryo-TEM has been extensively used to investigate the formation of self-assembled polymer nanostructures,[121-131] and it provides an avenue of obtaining time-resolved images.[132] This is enabled by freezing a thin layer of solution during the formation process on the EM grid, thereby trapping the evolving structures as a function of time. Although this approach can achieve sub-nanometer spatial resolution, the temporal resolution is limited due to the necessity of freezing separated samples at different stages of structure formation.[133] In contrast, significantly better temporal resolution can be obtained in *in situ* liquid phase TEM and STEM experiments (LP-EM). The dynamic processes that lead to the formation of inorganic nanoparticles (hard materials) in solution have been successfully imaged in LP-EM experiments. There are two different types of liquid cells. The conventional flow cell with silicon nitride windows is capable of exchanging the solution in the cell during imaging, while the novel graphene cell wraps a droplet containing reactants between two layers of graphene. The flow cell provides better control over solution concentration, a key parameter that affects structure formation.[134-135] In contrast, the graphene cell provides better spatial resolution due to the fact that the thicknesses of the sample and the windows are much lower, and due to the superior conductivity of graphene.[136-137] As shown in Figure 1A (first entry in Table 1), Ianiro *et al.*

applied low-dose LP-EM to characterize the vesicle formation in a flow cell.[138] The vesicle-forming system investigated was poly(ethylene oxide)-*b*-poly(caprolactone) (PEO-*b*-PCL) in water. The authors hypothesized that liquid–liquid phase separation was a precursor to vesicle formation. To test their hypothesis, they monitored the assembly process in real time by capturing a movie with temporal resolution of one frame per second. Figure 1A.1 shows the chemical structure of PEO-*b*-PCL. Figure 1A.2 shows a direct comparison of images of mature vesicles obtained by LP-EM (left panel) and cryo-TEM (right panel). The comparison shows that vesicles formed in the flow cell are identical to those formed under quiescent conditions. Figure 1A.3 shows a series of frames captured from the same vesicle during the formation process. The dark pixels represent the PEO-*b*-PCL block copolymer. The top row shows a time series of individual frames. In the early stage (first frame), it is difficult to distinguish between the pixels corresponding to the vesicle and those corresponding to the background. A patchy vesicle is seen in the second frame. The contrast of the vesicle and background is clear in the third frame, ultimately leading to the formation of a mature vesicle in the fourth frame. The bottom row shows a time series of 30-frame-averaged images; the time stamps for both the top and bottom row are the same. The averaged images are qualitatively different from the individual frames. The SNR in the individual frames is very low since only a few electrons are used to form each image. To improve SNR, the authors binned adjacent pixels but this results in a loss of high spatial frequency information. The first averaged image in the 30-frame-averaged time series shows that the vesicle precursor has a spherical morphology in the early stage. Both the single frame and 30-frame-averaged series indicate that the time scale for vesicle formation is about 900 seconds. An important feature of the vesicle membrane is the presence of hydrophilic polymer brush layers emanating from the hydrophobic core (bottom cartoon in Figure 1.A.1).

The resolution (about 140 Å) in this study is not sufficient to resolve this feature. Nevertheless, the dynamic process involved in vesicle formation were effectively captured by averaged low-dose *in situ* EM of unstained polymers with sufficiently high temporal and spatial resolution.

The structure of vesicles is relatively simple, when compared to other self-assembled structures due to its spherical symmetry. Micelles are another common class of self-assembled structures formed by amphiphilic block copolymers in solution.[139-140] Structural inhomogeneity and overlap of random orientations of micelles in solution hinder the accurate interpretation of 2D projections from cryo-TEM. In such cases, the 3D reconstructed tomograms obtained by cryo-ET are of great importance. Zhang *et al.* studied the structure of micelles comprising polymerized ionic liquids using cryo-TEM and cryo-ET as shown in Figure 1B (second entry in Table 1).[141] The poly(ionic liquids), which have a hydrophilic backbone with heterocyclic cations and alkylbromide anions, are shown in the top row of Figure 1B.1. The alkyl chain length was varied from C_{12} to C_{16}. These polymers form micelles in water as shown in the bottom part of Figure 1B.1. However, the alkyl backbones and charged side chains form separate microphases within the micelle. 2D projections of the micelles obtained with different alkyl side chains are shown in Figures 1B.2 to 4. The dark domains represent the electron dense hydrophilic portion of the side chains which contain bromine (or iodine) atoms. The improved resolution (about 30 Å) relative to Figure 1A enables the distinction of hydrophilic and hydrophobic phases in micelles. However, the overall shape of micelles cannot be discerned from the 2D projections, especially in Figures 1B.2 and 1B.4. The slices from tomograms of micelles shown in Figures 1B.5 and 1B.6 reveal the overall “wasp-like” or “onion-like” shapes of the micelles, depending on side-chain length. How the internal layers connect to the surface of the micelle can be seen in Figure 1B.5; this cannot be determined from 2D projections.

Structures of crystalline polymers depend strongly on the processing conditions. Poly(3-hexylthiophene), P3HT, is a widely studied semicrystalline polymer. The π–π stacking of the conjugated backbone induces the crystallization of P3HT chains in solid films obtained by solution processing using organic solvents. Energy filtered TEM has been successfully used to image P3HT phases in unstained solid films relevant to devices.[43, 142-143] It is, however, important to characterize the state of P3HT crystals in solution. Wirix *et al*. used cryo-ET to study the nature of crystalline P3HT ribbons in organic solvents (third entry in Table 1).[144] The structure and proposed packing scheme of P3HT molecules are shown in Figure 1C.1. It is noteworthy that the solvents used in this work, toluene and 1,2-dichlorobenzene (oDCB), are toxic. The standard process used to vitrify aqueous samples was modified and carried out in a fume hood to enable these experiments. The cryo-TEM 2D projection and the 3D reconstructed tomogram of a crystalline P3HT ribbon are shown in Figures 1C.2 and 3, respectively. The dark regions represent the electron dense backbones. The spacing between two dark regions is 1.7 nm which is the spacing between two backbones perpendicular to the plane of the ribbon. A slice from the tomogram shown in Figure 1C.4 shows a cross-section of a ribbon. Surprisingly, the tomogram contains straight and parallel lines representing the crystalline P3HT chains with curved and disordered P3HT chains emanating from the crystalline core. The cartoon in Figure 1C.5 depicts the ordered core and the disordered edges in a P3HT ribbon. Information about the disordered regions of the ribbons can only be observed in solution wherein the natural state is preserved in spite of high-resolution imaging; the resolution obtained in this study was 1.7 nm.

It should be clear that staining is not an option for any of the characterization studies covered in Figure 1. The same holds true for all of the examples covered in this review.

3. Heterogeneity of self-assembled polymer structures in solution

Inferences of molecular conformations in self-assembled structures require accurate determination of their shape and size. Cryo-TEM and cryo-ET imaging have been used to determine membrane geometries of vesicles formed by phospholipids and block copolymers.[145-147] However, heterogeneities within the membrane must be resolved before anticipative analysis of the molecular conformation is possible. This is accomplished by sorting and averaging local structures.

Polypeptoids are bio-inspired polymers comprising repeating N-substituted glycine monomer units. They are similar to polypeptides except for the fact that the side chain is appended to the nitrogen atom rather than the α-carbon.[148] Jiang *et al.* studied the membrane structure of self-assembled vesicles formed by sequence-defined amphiphilic, poly-N-(2-ethyl)hexylglycine-block-poly-N-phosphonomethylglycine (pNeh-*b*-pNpm) polypeptoid block copolymers in water (fourth entry in Table 1).[149] Figure 2A.1 shows the chemical structure of pNeh-*b*-pNpm. The morphology of the vesicles was characterized by low-dose cryo-TEM with contrast generated by defocus as shown in Figure 2A.2. Small boxes extracted from the vesicle membrane micrographs were sorted and averaged to quantify membrane heterogeneity. The algorithm used was a modified version of the algorithm used for single particle analysis developed by the structural biology community. The difference between averaging performed on this sample versus that described in Figure 1A is the use of sorting; the average in Figure 1A corresponds to a simple juxtaposition of frames obtained from the same structure. The left panel in Figure 2A.3 shows the spatial distribution of different classes superposed on the vesicle. Averaged images in Figure 2A.3 show two classes (1a, 1b and 2) with different membrane thicknesses in the right panel. The colors of box outlines, blue and aqua, indicate different

classes. In this case, the machine-learning-based sorting algorithm led to the identification of three classes but two of them (classes 1a and 1b) were very similar. It is evident that in this early stage of using machine-learning-based algorithms, it is sometimes necessary to combine the output of such algorithms with physical reasoning. Molecular dynamic simulations were used to interpret the averaged cryo-TEM images. Two models corresponding to a monolayer and a bilayer were developed and the relaxed simulation results are shown in Figure 2A.4. While it is clear that the grey curved regions in the micrographs represent the vesicle, the origin of the dark bands at the edges was unclear. Analysis of the computed images based on the atomic models in Figure 2A.4 indicated that the dark bands are part of hydrophobic core. They arise due to the necessity for using a defocused configuration and the concomitant presence of Fresnel fringes in the micrographs. The membranes formed by pNeh-*b*-pNpm are dominated by monolayers comprising interdigitated hydrophobic blocks that coexist with bilayers comprising tilted non-interdigitated hydrophobic blocks. Determination of molecular conformations in these vesicles was only possible after local heterogeneity was quantified by sorting and averaging of 2D micrographs.

The local heterogeneity in vesicles can be more complex than that pictured in Figure 2A. Cornell *et al*. demonstrated the coexistence of liquid-ordered (Lo) and liquid-disordered (Ld) phases in the membrane of vesicles formed by phospholipids, as shown in Figure 2B.1 (fifth entry in Table 1).[150] Unlike the 2D projections used for sorting and averaging in Figure 2A, these vesicles were analyzed by 3D cryo-ET data. Slices of the tomograms were used to measure the local membrane thickness in a vesicle. The analysis quantified the area fractions of two different configurations of the phospholipid as well as their spatial distributions. Figures 2B.2 and 2B.3 show the slices of the tomograms that indicate the heterogeneity of membrane structures

consisting of Lo (red) and Ld (blue) phases in a single vesicle, respectively. The graphs associated with these figures quantify the local variation of membrane thickness as a function of position.

This local structural information about the arrangement of molecules in the membrane is valuable for the investigation of membrane formation theories. Electron microscopy is ideally suited for obtaining this information relative to other characterization methods.

Messmer *et al*. applied cryo-TEM and cryo-ET to elucidate the molecular conformations of dendronized amphiphilic polymers (DPs) in micelles (sixth entry in Table 1).[151] Figure 2C.1 shows the micelle structure obtained from molecular dynamics (MD) simulations. The micelle comprises a thick hydrophilic shell formed by dendritic side chains and a thin hydrophobic spine formed by the core of dendrimer. Figure 2C.2 shows a cryo-TEM image of micelles in vitreous ice with inverted contrast. Projections of micelles selected for analysis in this particular image are shown in red. A large number of images, similar to Figure 2C.2, were analyzed using the single particle approach. The results of this analysis are shown in Figure 2C.3. Here we see 11 distinct classes with varying degrees of curvature. Messmer *et al*. also collected cryo-ET data and used the single particle approach for data analysis. The classes obtained by cryo-ET shown in Figure 2C.4 are indistinguishable from those obtained by cryo-TEM shown in Figure 2C.3. The local curvature of one of the cryo-ET classes are shown on the expanded scale in Figure 2C.5. The curved backbones in the micelles seen by electron microscopy cannot be properly explained by MD simulations. Acknowledging such discrepancies is an important first step for improving our understanding of the inter-atomic interactions that govern nanostructure formation; unfortunately, such discrepancies are rarely reported in literature.

4. Imaging crystalline soft materials at the atomic scale

High-resolution imaging at the atomic scale has the potential to reveal the geometry of crystalline unit cells, polymorphs, and grain boundaries in semicrystalline polymers. It should be evident that characterizing heterogeneity is essential for imaging on this length scale. TEM is routinely used to image two classes of materials with atomic resolution: hard crystalline materials such as metals by direct imaging and biological macromolecules such as proteins by sorting and averaging. In this section, we will discuss the cryo-TEM imaging of crystalline structures in two kinds of well-ordered synthetic soft materials: metal-organic frameworks and polypeptoids.

Metal-organic frameworks (MOFs) are highly porous materials whose physical and chemical properties can be tuned at the atomic level by engineering the coordination of metal ions and organic linkers.[152-153] The organic linkers found in MOFs are similar to those found in synthetic polymers. MOFs have been used as polymerization catalysts and fillers in polymer nanocomposites.[154-155] In addition, novel hybrid materials have been obtained by covalently bonding polymer chains to MOFs. [156-159]

X-ray diffraction (XRD) and micro electron diffraction (Micro-ED) conducted on crystals can be used to determine averaged crystal structure of MOF particles but the information about the phase difference between scattered beams from the constituent atoms is lost.[160-161] The presence of organic linkers results in the radiation sensitivity and low-dose TEM imaging is essential for preserving phase information. Patterson *et al*. studied the structure of neat MOF crystals and MOF-protein complexes using *in situ* LP-EM and *ex situ* low-dose cryo-TEM. They achieved a resolution of 13 Å using 5 $e/Å^2$ per image in the cryo-TEM study.[162-163] In a

subsequent study, Zhu *et al*. used a direct electron detector to improve the resolution to 2.1 Å.[164] The use of spherical aberration corrected TEM coupled with very low dose imaging, 3 e/Å^2 per image, enabled 1.4 Å resolution.[165] One of the major applications of MOF crystals is gas absorption. The first direct image of adsorbed gas molecules in MOF crystals was obtained by Li *et al*. (seventh entry in Table 1).[166] A ZIF-8 MOF crystal saturated with CO_2 was plunged into liquid ethane to trap the CO_2 molecules inside the crystal. A cartoon of the structure of ZIF-8 MOF crystal with a CO_2 guest molecule is shown in Figure 3A.1. The frozen MOF crystal is shown in Figure 3A.2. Figure 3A.3 shows the CTF-corrected denoised image obtained from the edge of the ZIF-8 MOF crystal in Figure 3A.2. The very bright regions correspond to electron-dense linkers and clusters in the crystal. Figure 3A.4 shows a magnified image from the region indicated by the red box in Figure 3A.3. The slight increasing brightness at the center of the cage suggests the presence of an absorbed CO_2 molecule within a ZIF-8 crystal. It is interesting to note that images in Figure 3A were obtained without sorting or averaging. The atomic scale imaging of lattice structure in a MOF crystal with CO_2 shows the potential of low-dose cryo-TEM for characterization of well-ordered organic structures.

Polypeptoid block copolymers are self-assembled in water to give crystalline nanosheets that serve as functional protein mimetics. Both the internal structure and surface properties of the nanosheets can be engineered at the atomic level.[167] Xuan *et al*. determined the structure of polypeptoid crystalline nanosheets at 1.5 Å resolution by cryo-TEM (eighth entry in Table 1).[168] The results from sorting and averaging indicated the presence of numerous distinct crystalline motifs (polymorphs). Quantitative analysis of the distribution of distinct crystal motifs indicated the correlations between neighboring unit cells and the growth mechanism of nanosheets at the

atomic level.[169-170] Other studies on semicrystalline polymers such as poly(paraxylylene)[25] and syndiotactic polystyrene,[171] have also suggested the presence of structural heterogeneity.

When the crystal is homogenous, averaging the identical crystal motifs significantly increases resolution. Figure 3B.1 shows the chemical structure of a amphiphilic polypeptoid with the hydrophilic poly(N-2-(2-(2-methoxyethoxy)ethoxy)ethylglycine) block and N-2-phenylethylglycine hydrophobic block with bromine atoms at the para position of phenyl rings (pNte-*b*-pNBrpe). The averaged cryo-TEM image of the crystalline nanosheets is shown in Figure 3B.2. Figure 3B.3 shows an MD simulation of a pNBrpe crystal. The peptoid chain backbones are orthogonal to the *a*-*c* plane shown in the Figure 3B.3. The correspondence between the averaged image and MD simulations is striking. The brightest feature in Figure 3B.2 represents the glycine backbone, while the two arms emanating the backbone represent the phenyl side chains. Each phenyl chain terminates in a grey spherical dot that represents the bromine atom. The Fourier transform of the image in Figure 3B.2, shown in Figure 3B.4, indicates resolution at 1.5 Å. This study shows the application of cryo-TEM and averaging method in the characterization of polymer crystals. The atomic details seen in Figure 3B.2 cannot be access by conventional scattering and imaging techniques.

5. Additional information-rich high-resolution imaging techniques

In the field of material science, STEM plays an important role in structure and property characterization. In contrast to the parallel beam used in TEM, a convergent beam is used to scan over the specimen and the transmitted electrons scattered at defined angles are recorded by annular detectors.[172] The contrast in the image obtained by conventional (high-angle) annular dark field STEM, (HA)ADF-STEM, is proportional to the square of the atomic number *Z* in a

thin specimen. HAADF-STEM and ADF-STEM are thus ideally suited for studying thin films of metal and semiconductors. There are, however, a few examples where these techniques have been used to study polymer thin films.[88, 173-181] The presence of light elements in these systems complicates the interpretation of scattering signals.

As compared to conventional STEM, TEM with direct electron detectors is more dose-efficient for phase contrast imaging, and polymers are extremely beam sensitive.[182] A recent breakthrough in the field of STEM imaging of polymers was enabled by the development of ultra-fast direct electron detectors and new algorithms for analyzing data. This approach is called four-dimensional STEM (4DSTEM). It uses a focused electron beam that is rastered across the sample and a diffraction pattern is acquired at each scan position. The dataset thus acquired contains a large number of individual convergent beam electron diffraction (CBED) patterns. This dataset provides comprehensive information regarding structure,[183] orientation,[184] localized lattice strain,[185] and other material properties.[186] 4DSTEM has been used to visualize the crystalline orientation in semicrystalline polymers[187-188] and peptide nanocrystals.[189] In addition to the amplitude information of the structure factor in the diffraction pattern, the phase information can be retrieved by reconstructing the information in CBED patterns by using integrated differential phase contrast (iDPC) and ptychography methods.[190,191]

Panova *et al*. studied the arrangement of organic semiconductor molecules (short polymer chain) using low-dose cryogenic 4DSTEM (ninth entry in Table 1).[188] The study covered reciprocal space up to 3.7 Å using 100 Å steps in position space. The chemical structure of the molecule, poly[2,5-bis(3-tetradecylthiophen-2-yl) thieno[3,2-b]thiophene] (PBTTT), is shown in Figure 4A.1. Thin films of this polymer were studied, as-cast and after annealing. By identifying the diffraction spots in the CBED disk, the orientations of polymer backbones were

determined at each real space probe location. Figure 4A.2 shows the orientation maps of the as-cast (left panel) and annealed (right panel) PBTTT thin films. The colors represent different orientations as defined by the inset color ring. Figure 4A.3 shows the backbone orientation maps of the as-cast (left panel) and annealed (right panel) PBTTT thin films, respectively. It is evident that grains with long-range order appear only after annealing. This study shows how structure–property relationships can be visualized in unstained polymers by exploiting techniques that were originally developed for hard materials.

An iDPC-STEM image is reconstructed by measuring the momentum changes of the electrons recorded on a segmented or a pixelated detector. The image contrast is proportional to the atomic number *Z* in a thin specimen.[192,193] While iDPC-STEM is often used to study dose-tolerant hard materials, recent advances have enabled visualizing light elements such as hydrogen and lithium atoms in crystalline solids.[193,194] This feature of iDPC-STEM could benefit the characterization of morphologies and structures in unstained polymers over a large range of length scales. More recently, Inamoto *et al*. demonstrated iDPC imaging of phase-separated structures in a poly (3-hexylthiophene) (P3HT) and [6,6]-phenyl-C61-butyric acid methyl ester (PCBM) blend without staining.[195] iDPC imaging increases the contrast between different components in the blend relative to conventional STEM. They also showed the iDPC-STEM tomography reconstruction of unstained acrylonitrile-butadiene-styrene (ABS) copolymer blended with an inorganic filler. The spatial distribution of the filler was visualized at the micrometer scale.[196]

Shen *et al*. determined the structure of a MIL-101 MOF crystal using low-dose spherical aberration corrected iDPC-STEM imaging at room temperature with accumulated dose up to 40 e/Å^2 (tenth entry in Table 1).[197] Figure 4B.1 shows the chemical structure of a MIL-101 MOF

crystal which contains Cr clusters and organic linkers. Figure 4B.2 shows an iDPC-STEM image of a MIL-101 MOF crystal. The bright regions represent the electron dense linkers and metal clusters. The corresponding Fourier transform of this image is shown in Figure 4B.3, where the reflections at 1.8 Å are clearly observed. The magnified high-resolution image obtained by averaging 30 iDPC-STEM images is show in the top panel in Figure 4B.4. The red and blue circles indicate the presence of two types of cages with 29 and 34 Å sizes. This is in good agreement with the atomic model shown in the bottom panel of Figure 4B.4. The direct visualization of local structures allows for better understanding of the node-linker coordination and the structure-property relations in MOFs. The local structures, including the surfaces, interfaces and defects in MOF crystals, were also revealed by low-dose HRTEM and low-dose STEM imaging. Li *et al*. studied MIL-101 MOF crystals using both low-dose iDPC-STEM and low-dose HRTEM.[198] As compared with the HRTEM image, the iDPC-STEM image exhibited slightly lower resolution but stronger contrast. The ability to image organic linkers in MOFs suggests the possibility of using iDPC-STEM to image polymers that only contain light elements.

Machine-learning, which was used in several studies that were discussed above, will undoubtedly play an increasingly significant role in electron microscopy. Modern direct electron detectors and imaging techniques generate large data sets such as dose-fractionation movies, tomograms, and diffraction pattern stacks. In the past, these data sets were analyzed using reference-free machine-learning algorithms. However, machine-learning-based methods, wherein algorithms are trained using large data sets are becoming increasingly popular. These methods use artificial neural networks for processing images in both position and reciprocal space. They have been used to track the symmetry and atomic positions in 2D systems such as

graphene and quantum materials,[199-200] increase signal-to-noise ratio,[201] identify the location of protein molecules in vitrified suspensions,[202] determine molecular conformations from discrete images,[203] segregate tomogram into separate phases,[204-205] and to quantify the shape and size of nanoparticles in a polymer composite.[206] The application of machine-learning-based image analysis is still rare in polymer science. One reason is the lack of databases that contain prior knowledge of structures formed by specific or similar polymers. Another reason is the presence of intrinsic heterogeneity in the structures formed by synthetic polymers on the atomic and nanometer length scales. Establishing appropriate databases will provide a foundation for utilizing the recent advances in high-resolution electron microscopy for characterization of synthetic polymers.

6. Conclusion

Electron microscopy is a powerful and versatile tool for the characterization of polymer nanostructures. Recent advances in hardware and software have enabled high-resolution imaging of unstained polymers. Low-dose imaging preserves the natural state of the specimen, but sorting and averaging independent images is essential for high-resolution. Based on the analysis of structural information in 2D projections, 3D tomograms and 4DSTEM datasets, structures formed by microphase separation or crystallization can be characterized at the nanoscale and, in some cases, at the atomic-scale. Time-resolved imaging can reveal the dynamics of complex processes such as vesicle formation. High spatial resolution imaging of local structures can reveal molecular conformations of amphiphilic block copolymers in self-assembled nanostructures including micelles. Atomic-scale imaging of polypeptoid and MOF crystals may open the door to atomically defined 2D and 3D nanostructures.

This review begins with a description of TEM results. We first present images obtained by simple averaging of low-dose 2D images of a block copolymer vesicle, resulting in images resolved at 140 Å (system 1). This is followed by a more sophisticated averaging of micelles formed by polymerized ionic liquids in water based on 3D tomograms, demonstrating improved resolution of 30 Å (system 2). Higher resolution (1.7 Å) was obtained in a solution of P3HT chains, wherein the crystalline core of nanowires was distinguished from amorphous structures on the fringes (systems 3). Heterogeneity on the 10 Å length scale within individual vesicles was studied in both diblock copolymers and lipid vesicles using sorting and averaging (systems 4 and 5). Micelles formed by dendronized polymers also exhibited heterogeneity, and a similar approach led to images of individual classes (system 6). Direct imaging of a MOF crystal under low-dose conditions enabled approaching the atomic-scale (system 7) in spite of the presence of organic linkers due to the presence of excellent long-range order. In contrast, sorting and averaging algorithms were necessary to obtain 1.5 Å resolution of a polypeptoid crystal (system 8). The review ends with a discussion of results obtained by STEM imaging techniques. We discuss the emerging technique of 4DSTEM, where images of a conjugated polymer (system 9) are created by collecting 2D diffraction data as a function of position (in 2D space). This is followed by the image of a MOF crystal obtained by iDPC-STEM (system 10), a technique that has not yet been applied to the high-resolution imaging of polymers.

New developments in related fields have the potential to further improve high-resolution imaging of unstained polymers. For example, Volta phase plates[207] and ultra-stable supporting grids[208] have not yet been used for imaging polymers. Ultra-fast tomography wherein projections are obtained on a direct electron detector while the sample is continuously tilted can reduce beam damage.[209-210] Low-dose 4DSTEM has the potential to directly image the nanoscale morphology

of polymer systems with atomic resolution. All these approaches will benefit from recently developed high speed pixelated direct electron detectors.[211]

Conflicts of interest:

The authors declare no competing financial interest.

Acknowledgements:

Funding for this work was provided by the Soft Matter Electron Microscopy Program (KC11BN), supported by the Office of Science, Office of Basic Energy Science, US Department of Energy, under Contract DE-AC02-05CH11231. Work at the Molecular Foundry was supported by the Office of Science, Office of Basic Energy Sciences, of the U.S. Department of Energy under Contract No. DE-AC02-05CH11231. We gratefully acknowledge the help provided from many discussions with Dr. Robert M. Glaeser and Dr. Bong-Gyoon Han at the Lawrence Berkeley National Laboratory.

Table 1. Summary of examples with microphase separated or crystalline structures

Materials	Morphology	Post-processing	Imaging method	Contrast	Accumulative electron dose (e Å^{-2})	Resolution (Å)	Retrieved information	Figures
(1) Diblock copolymer	Vesicle	Simple averaging	In-situ liquid cell TEM	Phase	0.006 e Å^{-2} per image	140	Dynamic morphological changes	Figure 1A, ref 138
(2) Poly(ionic liquid)	Micelle	Tomographic 3D reconstruction	Cryo-ET	Phase	100 e Å^{-2} for tilt series	30	Morphological changes and chain conformation	Figure 1B, ref 141
(3) Conjugated polymer P3HT	Crystalline nanowire	Tomographic 3D reconstruction	Cryo-ET	Phase	2000 e Å^{-2} for tilt series[2]	17	Ordered and disordered regions in nanowire	Figure 1C, ref 144
(4) Diblock copolypeptoid	Vesicle	Sorting and averaging	Cryo-TEM	CTF corrected phase	30 e Å^{-2} per image	10	Membrane structure, chain conformation and inhomogeneity	Figure 2A, ref 149
(5) Lipid	Vesicle	Tomographic 3D reconstruction and sorting	Cryo-TEM	CTF corrected phase	74-100 e Å^{-2} for tilt series	10	Membrane structure, chain conformation and inhomogeneity	Figure 2B, ref 150
(6) Dendronized polymers	Micelle	Single particle 3D reconstruction	Cryo-ET	CTF corrected phase	180 e Å^{-2} for tilt series	10	Backbone conformation	Figure 2C, ref 151
(7) MOF, ZIF-8	3D crystal	Direct imaging	Cryo-TEM	CTF corrected phase	6.8 e Å^{-2} per image	1.8	Lattice structure	Figure 3A, ref 166
(8) Polypeptoid block copolymer	Crystalline nanosheet	Averaging	Cryo-TEM	CTF corrected phase	20 e Å^{-2} per image	1.5	Lattice structure ,backbone and side chain packing	Figure 3B, ref 168
(9) Conjugated polymer PBTTT	Microphase separation	Reconstructed diffractions	Cryo 4D-STEM	Diffraction	100 e Å^{-2} per diffraction	3.7	Orientation of crystals, the degree of crystallinity and grain boundary	Figure 4A, ref 188
(10) MOF, MIL-101	3D crystal	Averaging	iDPC-STEM	Reconstructed phase [1]	40 e Å^{-2} per image	1.8	Lattice structure	Figure 4B, ref 197

1. The phase is reconstructed based on the method reported in ref 193.
2. Aromatic molecules are less radiation sensitive than aliphatic molecules. Detailed discussion can be found in ref 37 and ref 52.

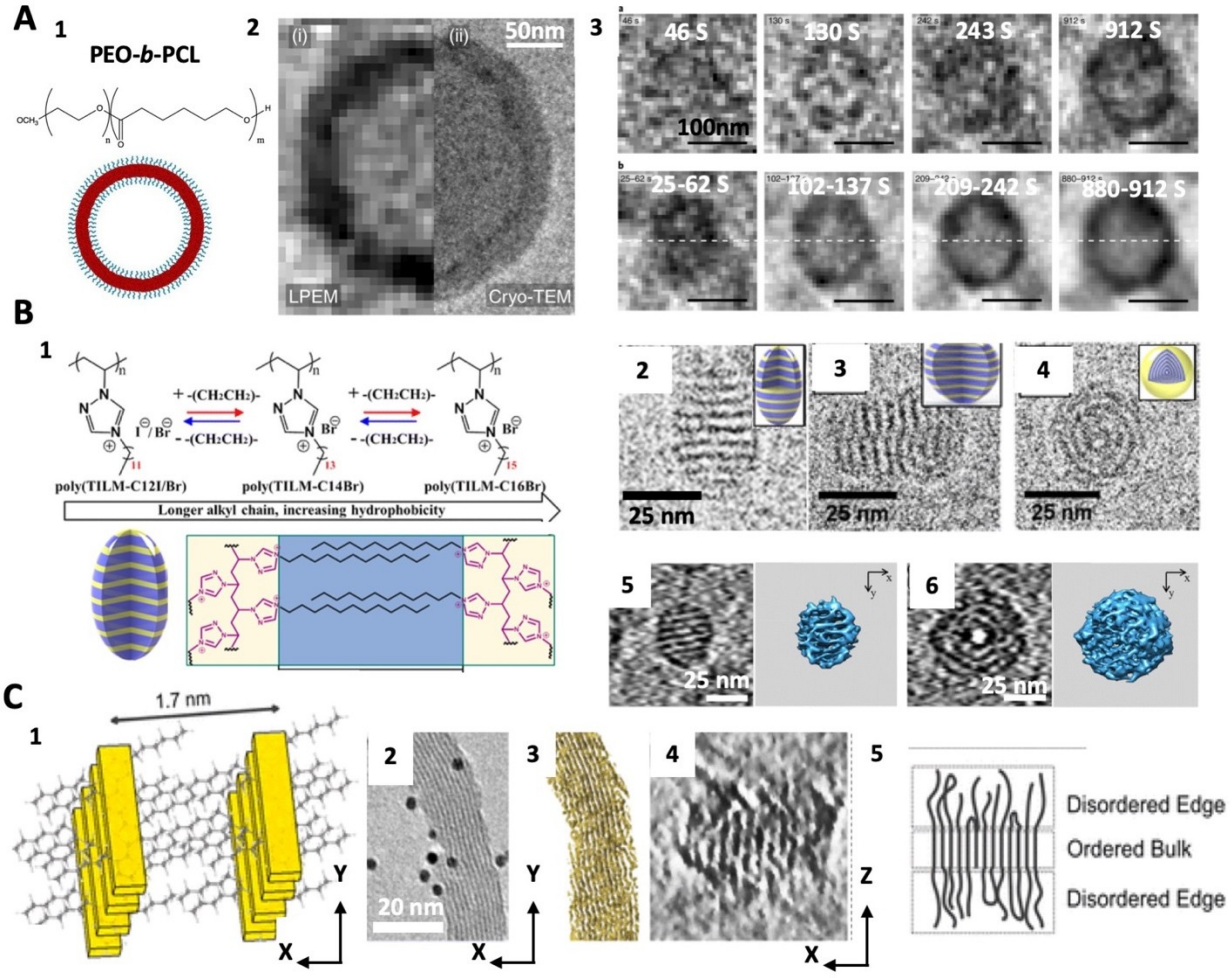

Figure 1. **A.** (1) The chemical structure of PEO-*b*-PCL and a schematic of the vesicle structure. (2) A comparison of a mature vesicle imaged by LP-EM (left) and cryo-TEM (right). (3) A comparison of an individual frame time series (top row) with a 30-frame-averaged time series (bottom row). Reproduced from ref 138 with permission. Copyright 2019 Springer Nature. **B**. (1) The chemical structures of the poly(ionic liquids) and a schematic of micelles comprising a microphase separated lamellar structure. Cryo-TEM images of micelles formed by poly(ionic liquids) with different alkyl side chains: (2) poly(TILM-C12I), (3) poly(TILM-C14Br), (4) poly(TILM-C16Br). Central tomographic slices along the *x*-*y* plane of the tomograms of (5)

poly(TILM-C12Br) and (6) poly(TILM-C16Br) micelles. 3D visualizations are shown in the right panels. Reproduced from ref 141 with permission. Copyright 2016 American Chemical Society. **C.** (1) Model of molecule arrangement within a P3HT nanowire. The yellow bars represent polymer backbone. (2) Cryo-TEM image of a P3HT nanowire vitrified in oDCB. Dark spheres are colloid gold nanoparticles used for the purpose of alignment. (3) The 3D visualized tomogram of the nanowire in 2. (4) Slice shows the *x*-*z* direction in the tomogram of the nanowire in 2. (5) A schematic depicts the ordered core and the disordered edges in 4. Reproduced from ref 144 with permission. Copyright 2014 American Chemical Society.

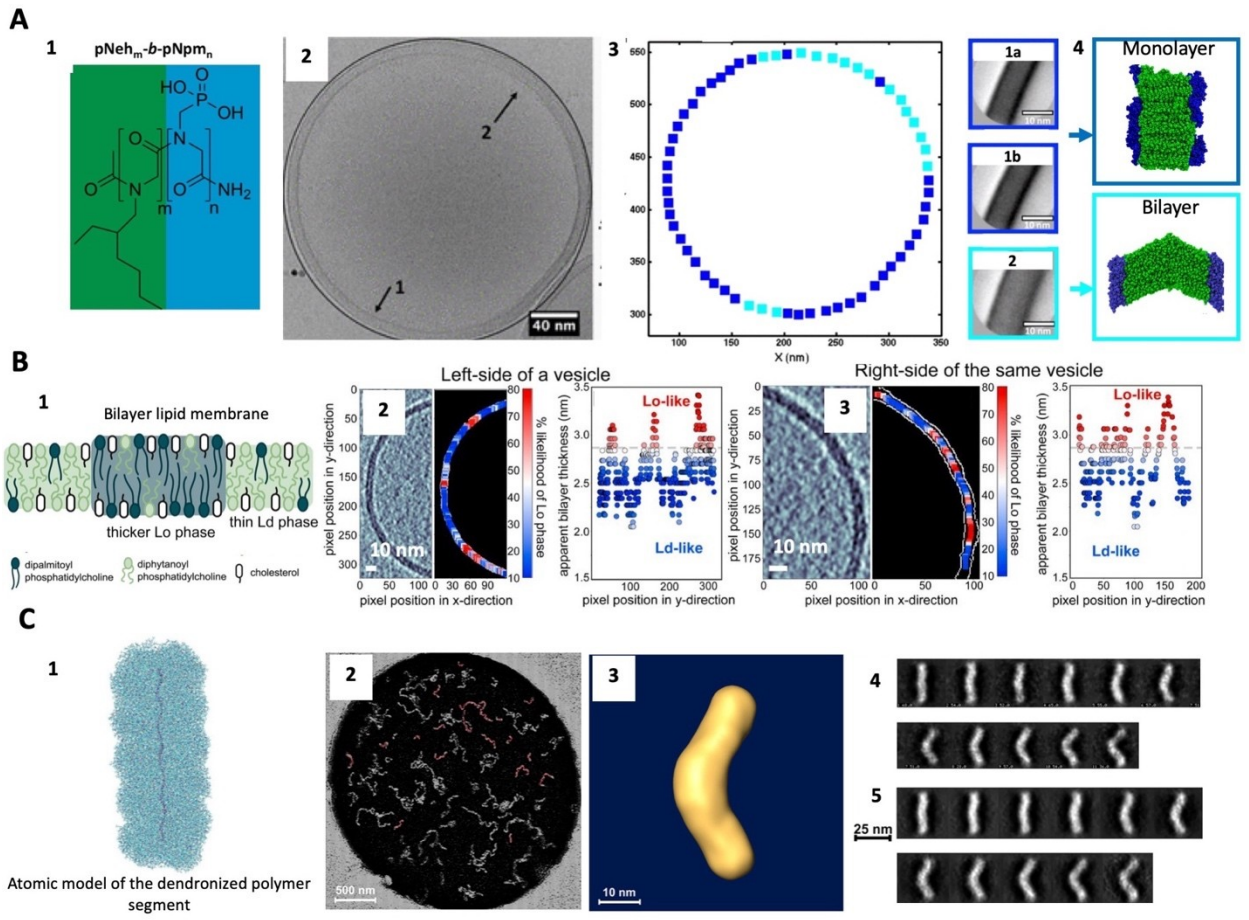

Figure 2. A. (1) The chemical structure of the pNeh-*b*-pNpm polypeptoid block copolymer that formed vesicles in water. Blue and green represent the hydrophilic and hydrophobic blocks, respectively. (2) Cryo-TEM image of a frozen hydrated vesicle formed by polypeptoid molecules. Arrows indicate the positions with different membrane thicknesses. A dark circle is drawn on the figure for reference. (3) The locations of the boxes belonging to different classes along the vesicle perimeter are shown in the left panel. Averaged high-resolution electron micrographs of boxes extracted from vesicles are shown in the right panel. Classes 1a and 1b have similar membrane thicknesses (collectively class 1) while class 2 has a larger membrane thickness. Two classes (represented by blue and aqua squares in the left panel). (4). MD simulations show the interdigitated monolayer packing (top) and tilted bilayer packing of the

pNeh-*b*-pNpm molecules in the membrane (bottom). The blue boxes in (3) represent the monolayer while the aqua boxes in (3) represent the bilayer. Reproduced from ref 149 with permission. Copyright 2018 American Chemical Society. **B.** (1). A schematic of a lipid membrane with coexisting liquid-ordered (Lo) and liquid-disordered (Ld) phases. The Lo phase is thicker than the Ld phase. Locations of Lo and Ld phases in the membrane of a vesicle are identified by analyzing the tomogram slices in the left panel in (2) Colors represent the likelihood (from 0 to 100%) that each location corresponds to the thicker, Lo, phase instead of the thinner, Ld, phase. A horizontal dashed line in the right panel shows the apparent bilayer thickness for which there is a 50% likelihood of being in the Lo phase. The analysis on the right side of the same vesicle is shown in (3) Reproduced from ref 150 with permission. Copyright 2020 National Academy of Sciences. **C.** (1) The structure of a micelle comprising short dendronized polymers (DPs) obtained from MD simulations. (2) Cryo-TEM image of micelles in vitrified 1,4-dioxane (inverted contrast). Micelles used for 3D reconstruction shown in red. (3) The 3D morphology of a segment of a micelle reconstructed from 896 different segments of the micelles colored in red in (2). The segments in this example correspond to boxes in (1). Averaged images of different classes of the micelle segment shown in (3) representing different viewing angles by 2D cryo-TEM (4) and projection of 3D cryo-ET (5). Reproduced from ref 151 with permission. Copyright 2019 American Chemical Society.

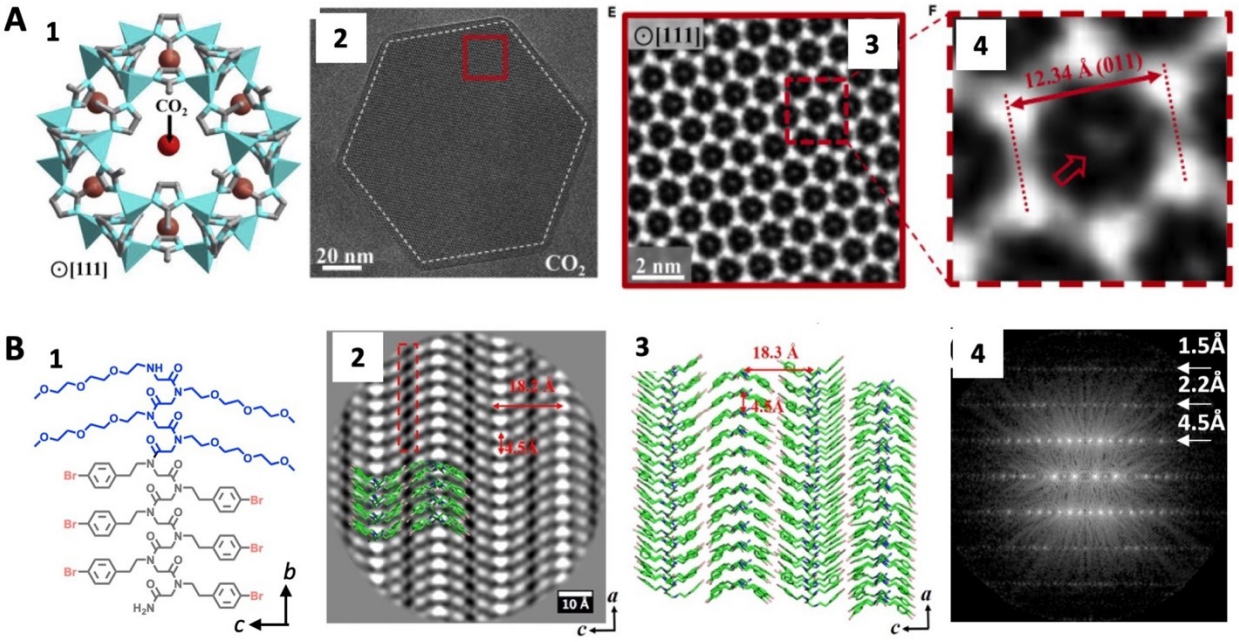

Figure 3. A. (1) Simulated structure of a ZIF-8 MOF crystal with DFT-predicted binding site of CO_2 (simplified as a red sphere) along the [111] projection. (2) Cryo-TEM image of a CO_2-filled ZIF-8 MOF crystal (outlined by white dashed lines) along the [111] projection. (3) CTF-corrected image of the red boxed region from (2). Bright regions correspond to electron dense metal clusters and organic linkers. (4) Magnified image of a single unit cell from (3). The grey region at the center of the unit cell (indicated by red arrow) corresponds to an adsorbed CO_2 molecule. Reproduced from ref 166 with permission. Copyright 2019. Elsevier Inc. **B.** (1) The chemical structure of a polypeptoid diblock copolymer (pNeh-*b*-pNBrpe) with Br atoms. (2) Averaged cryo-TEM image of nanosheets formed by pNeh-*b*-pNBrpe in water. The Br atoms are are seen as grey dots at the end of the side chains; the brightest regions represent the glycine backbone. (3) Top view of the simulated nanosheet in water. A portion of the simulation box is superposed on the the cryo-TEM image shown in (2). (4) A Fourier transform of the image in

(2). Reflections are visible up to 1.5 Å (top row). Reproduced from ref 168 with permission. Copyright 2019. National Academy of Sciences of the United States of America.

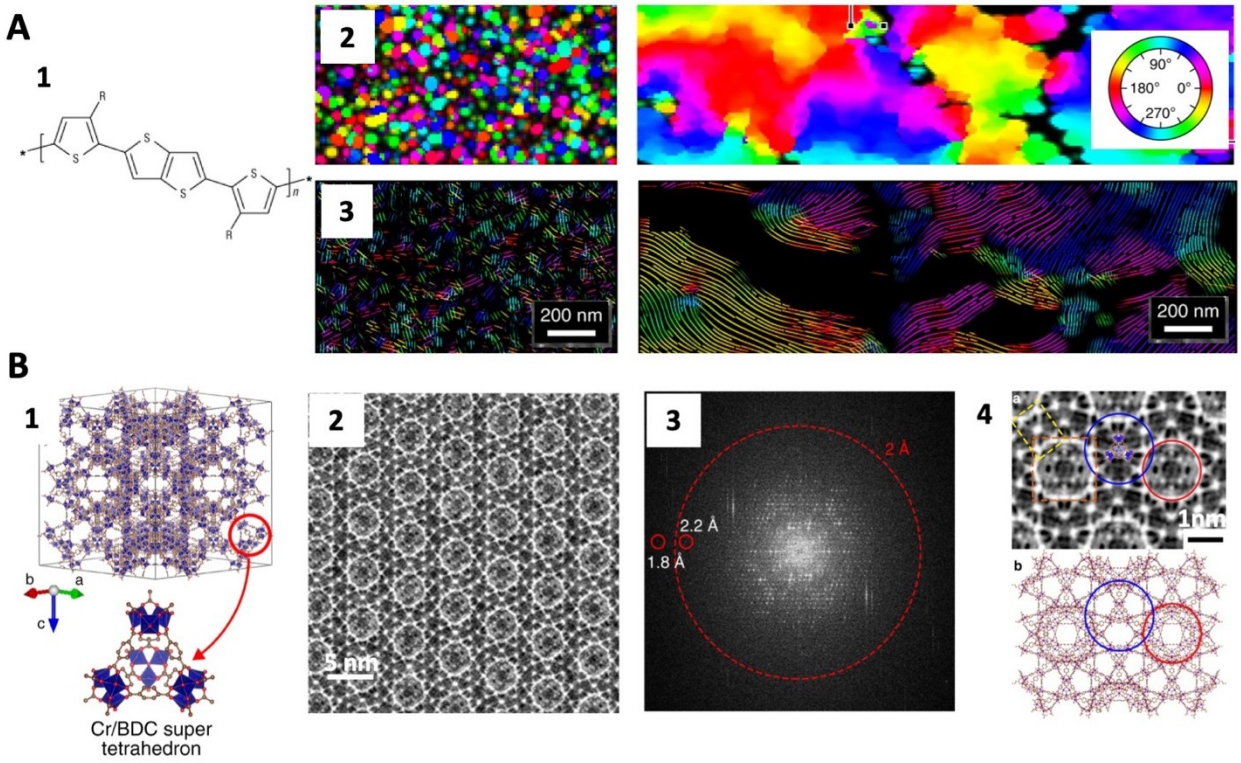

Figure 4. A. (1). The chemical structure of a PBTTT molecule. (2). Reconstruction maps show the orientation of crystals in the as-cast (left) and annealed (right) PBTTT thin films, respectively. (3). Reconstruction maps show the flowline of backbones in the as-cast (left) and annealed (right) PBTTT thin films, respectively. Reproduced from ref 188 with permission. Copyright 2019 Springer Nature. **B.** (1) The framework model of a MIL-101 MOF crystal. (2) An iDPC-STEM image of a MIL-101 MOF crystal. (3) The corresponding Fourier transform of the image shown in (2) with reflections up to 1.8 Å. (4) The averaged iDPC-STEM image of a MIL-101 MOF crystal. (top) and the atomic model (bottom). The red and blue circles indicate

two types of cages with 29 and 34 Å sizes, respectively. Reproduced from ref 197 with permission. Copyright 2020 Springer Nature.

References:

1. Wunderlich, B., *Macromolecular Physics*. Rensselaer Polytechnic Institute, Troy, New York: **1976.**
2. Leibler, L., Theory of Microphase Separation in Block Copolymers. *Macromolecules* **1980,** *13*, 1602-1617.
3. Feng, X. Y.; Burke, C. J.; Zhuo, M. J.; Guo, H.; Yang, K. Q.; Reddy, A.; Prasad, I.; Ho, R. M.; Avgeropoulos, A.; Grason, G. M.; Thomas, E. L., Seeing mesoatomic distortions in soft-matter crystals of a double-gyroid block copolymer. *Nature* **2019,** *575*, 175-175.
4. Cochran, E. W.; Garcia-Cervera, C. J.; Fredrickson, G. H., Stability of the gyroid phase in diblock copolymers at strong segregation. *Macromolecules* **2006,** *39*, 2449-2451.
5. Bates, F. S.; Maurer, W. W.; Lipic, P. M.; Hillmyer, M. A.; Almdal, K.; Mortensen, K.; Fredrickson, G. H.; Lodge, T. P., Polymeric bicontinuous microemulsions. *Phys Rev Lett* **1997,** *79*, 849-852.
6. Matsen, M. W.; Bates, F. S., Unifying weak- and strong-segregation block copolymer theories. *Macromolecules* **1996,** *29*, 1091-1098.
7. Hajduk, D. A.; Harper, P. E.; Gruner, S. M.; Honeker, C. C.; Kim, G.; Thomas, E. L.; Fetters, L. J., The Gyroid - a New Equilibrium Morphology in Weakly Segregated Diblock Copolymers. *Macromolecules* **1994,** *27*, 4063-4075.
8. Tan, K. W.; Wiesner, U., Block Copolymer Self-Assembly Directed Hierarchically Structured Materials from Nonequilibrium Transient Laser Heating. *Macromolecules* **2019,** *52*, 395-409.
9. Bates, F. S.; Fredrickson, G. H., Block copolymers - Designer soft materials. *Phys Today* **1999,** *52*, 32-38.
10. Bates, F. S., Polymer-Polymer Phase-Behavior. *Science* **1991,** *251*, 898-905.
11. Jinnai, H.; Nishikawa, Y.; Spontak, R. J.; Smith, S. D.; Agard, D. A.; Hashimoto, T., Direct measurement of interfacial curvature distributions in a bicontinuous block copolymer morphology. *Phys Rev Lett* **2000,** *84*, 518-521.
12. Thomas, E. L.; Anderson, D. M.; Henkee, C. S.; Hoffman, D., Periodic Area-Minimizing Surfaces in Block Copolymers. *Nature* **1988,** *334*, 598-601.
13. Ruska, E., The Development of the Electron-Microscope and of Electron-Microscopy. *Rev Mod Phys* **1987,** *59*, 627-638.
14. Storks, K. H., An electron diffraction examination of some linear high polymers. *J Am Chem Soc* **1938,** *60*, 1753-1761.
15. Agar, A. W.; Frank, F. C.; Keller, A., Crystallinity Effects in the Electron Microscopy of Polyethylene. *Philos Mag* **1959,** *4*, 32-55.

16. Cooper, A. C.; Keller, A.; Waring, J. R. S., Texture of Some Crystalline Synthetic Polymers by Electron Microscopy. *J Polym Sci* **1953,** *11*, 215-220.
17. Keller, A.; Oconnor, A., Study of Single Crystals and Their Associations in Polymers. *Discuss Faraday Soc* **1958**, 114-121.
18. Keller, A.; Keller, A.; Engleman, R., Electron Microscope-Electron Diffraction Investigations of the Crystalline Texture of Polyamides. *J Polym Sci* **1959,** *36*, 361-387.
19. Sauer, J. A.; Morrow, D. R.; Richards.Gc, Morphology of Solution-Grown Polypropylene Crystal Aggregates. *J Appl Phys* **1965,** *36*, 3017-3021.
20. Dlugosz, J.; Keller, A.; Pedemont.E, Electron Microscope Evidence of a Macroscopic Single Crystal from a 3-Block Copolymer. *Kolloid Z Z Polym* **1970,** *242*, 1125-1130.
21. Grubb, D. T.; Groves, G. W.; Keller, A., Origin of Contrast Effects in Electron-Microscopy of Polymers .1. Polyethylene Single-Crystals. *J Mater Sci* **1972,** *7*, 131-141.
22. Moss, B.; Dorset, D. L.; Wittmann, J. C.; Lotz, B., Electron Crystallography of Epitaxially Grown Paraffin. *J Polym Sci Pol Phys* **1984,** *22*, 1919-1929.
23. Dorset, D. L., Crystal-Structure of Lamellar Paraffin Eutectics. *Macromolecules* **1986,** *19*, 2965-2973.
24. Dorset, D. L., Direct Structure-Analysis of a Paraffin Solid-Solution. *P Natl Acad Sci USA* **1990,** *87*, 8541-8544.
25. Pradere, P.; Thomas, E. L., Image-Processing of Partially Periodic Lattice Images of Polymers - the Study of Crystal Defects. *Ultramicroscopy* **1990,** *32*, 149-168.
26. Martin, D. C.; Thomas, E. L., Experimental High-Resolution Electron-Microscopy of Polymers. *Polymer* **1995,** *36*, 1743-1759.
27. Wittmann, J. C.; Lotz, B., Polymer Decoration - the Orientation of Polymer Folds as Revealed by the Crystallization of Polymer Vapors. *J Polym Sci Pol Phys* **1985,** *23*, 205-226.
28. Tosaka, M.; Tsuji, M.; Kohjiya, S.; Cartier, L.; Lotz, B., Crystallization of syndiotactic polystyrene in beta-form. 4. Crystal structure of melt-grown modification. *Macromolecules* **1999,** *32*, 4905-4911.
29. Zhu, L.; Cheng, S. Z. D.; Calhoun, B. H.; Ge, Q.; Quirk, R. P.; Thomas, E. L.; Hsiao, B. S.; Yeh, F. J.; Lotz, B., Crystallization temperature-dependent crystal orientations within nanoscale confined lamellae of a self-assembled crystalline-amorphous diblock copolymer. *J Am Chem Soc* **2000,** *122*, 5957-5967.
30. Huang, P.; Zhu, L.; Cheng, S. Z. D.; Ge, Q.; Quirk, R. P.; Thomas, E. L.; Lotz, B.; Hsiao, B. S.; Liu, L. Z.; Yeh, F. J., Crystal orientation changes in two-dimensionally confined nanocylinders in a poly(ethylene oxide)-b-polystyrene/polystyrene blend. *Macromolecules* **2001,** *34*, 6649-6657.
31. Zhu, L.; Cheng, S. Z. D.; Calhoun, B. H.; Ge, Q.; Quirk, R. P.; Thomas, E. L.; Hsiao, B. S.; Yeh, F.; Lotz, B., Phase structures and morphologies determined by self-organization, vitrification, and crystallization: confined crystallization in an ordered lamellar phase of PEO-b-PS diblock copolymer. *Polymer* **2001,** *42*, 5829-5839.
32. Lotz, B.; Miyoshi, T.; Cheng, S. Z. D., 50th Anniversary Perspective: Polymer Crystals and Crystallization: Personal Journeys in a Challenging Research Field. *Macromolecules* **2017,** *50*, 5995-6025.
33. Handlin, D. L.; Thomas, E. L.; Macknight, W. J., Critical-Evaluation of Electron-Microscopy of Ionomers. *Macromolecules* **1981,** *14*, 795-801.

34. Pradere, P.; Thomas, E. L., 3-Dimensional Model for Twinning in Polymer Single-Crystals with Inclined Chains. *Philos Mag A* **1989,** *60*, 177-203.
35. Sadler, D. M.; Keller, A., Polyethylene Crystals with Dislocation Networks - Their Origin Structure and Relevance to Polymer Crystallization .2. *Kolloid Z Z Polym* **1970,** *242*, 1081-&.
36. Glaeser, R. M., Limitations to Significant Information in Biological Electron Microscopy as a Result of Radiation Damage. *J Ultra Mol Struct R* **1971,** *36*, 466-&.
37. Egerton, R. F.; Li, P.; Malac, M., Radiation damage in the TEM and SEM. *Micron* **2004,** *35*, 399-409.
38. Glaeser, R. M., Retrospective: Radiation damage and its associated "Information Limitations". *Journal of structural biology* **2008,** *163*, 271-276.
39. Leijten, Z. J. W. A.; Keizer, A. D. A.; de With, G.; Friedrich, H., Quantitative Analysis of Electron Beam Damage in Organic Thin Films. *J Phys Chem C* **2017,** *121*, 10552-10561.
40. Koshino, M.; Masunaga, Y. H.; Nemoto, T.; Kurata, H.; Isoda, S., Radiation damage analysis of 7,7,8,8,-tetracyanoquinodimethane (TCNQ) and 2,3,5,6,-tetrafluoro-7,7,8,8,-tetracyanoquinodimethane (F(4)TCNQ) by electron diffraction and electron energy loss spectroscopy. *Micron* **2005,** *36*, 271-279.
41. Hayashida, M.; Kawasaki, T.; Kimura, Y.; Takai, Y., Estimation of suitable condition for observing copper-phthalocyanine crystalline film by transmission electron microscopy. *Nucl Instrum Meth B* **2006,** *248*, 273-278.
42. Eggeman, A. S.; Illig, S.; Troisi, A.; Sirringhaus, H.; Midgley, P. A., Measurement of molecular motion in organic semiconductors by thermal diffuse electron scattering. *Nat Mater* **2013,** *12*, 1044-1048.
43. Guo, C. H.; Allen, F. I.; Lee, Y.; Le, T. P.; Song, C.; Ciston, J.; Minor, A. M.; Gomez, E. D., Probing Local Electronic Transitions in Organic Semiconductors through Energy-Loss Spectrum Imaging in the Transmission Electron Microscope. *Adv Funct Mater* **2015,** *25*, 6071-6076.
44. Kuei, B.; Bator, C.; Gomez, E. D., Imaging 0.36 nm Lattice Planes in Conjugated Polymers by Minimizing Beam Damage. *Macromolecules* **2020,** *53*, 8296-8302.
45. Kuei, B.; Gomez, E. D., Pushing the limits of high-resolution polymer microscopy using antioxidants. *Nat Commun* **2021,** *12*, 153.
46. Grubb, D. T., Review Radiation-Damage and Electron-Microscopy of Organic Polymers. *J Mater Sci* **1974,** *9*, 1715-1736.
47. Glaeser, R. M., Downing, K., Chiu, W., DeRosier, D., Frank, J., *Electron crystallography of biological macromolecules*. Oxford University Press: Oxford ; New York, **2007**.
48. Giorgio, S.; Kern, R., High-Resolution Electron-Microscopy of Polyethylene and Paraffin Crystals - Stability in the Electron-Beam. *J Polym Sci Pol Phys* **1984,** *22*, 1931-1951.
49. Dorset, D. L.; Zemlin, F., Direct Phase Determination in Electron Crystallography - the Crystal-Structure of an Normal-Paraffin. *Ultramicroscopy* **1990,** *33*, 227-236.
50. Dorset, D. L.; Zhang, W. P., Electron Crystallography at Atomic Resolution - the Structure of the Odd-Chain Paraffin Normal-Tritriacontane. *J Electron Micr Tech* **1991,** *18*, 142-147.

51. Glaeser, R. M.; McMullan, G.; Faruqi, A. R.; Henderson, R., Images of paraffin monolayer crystals with perfect contrast: minimization of beam-induced specimen motion. *Ultramicroscopy* **2011,** *111*, 90-100.
52. Glaeser, R. M., Chapter Two - Specimen Behavior in the Electron Beam. In *Methods in Enzymology*, Crowther, R. A., Ed. Academic Press: **2016,** 579, 19-50.
53. Fryer, J. R., Radiation-Damage in Organic Crystalline Films. *Ultramicroscopy* **1984,** *14*, 227-236.
54. Egerton, R. F., Control of radiation damage in the TEM. *Ultramicroscopy* **2013,** *127*, 100-108.
55. Janicek, B.; Kharel, P.; Bae, S. h.; Huang, P., Quantifying the Protection Factor of Graphene Substrates for Atomic-scale Imaging of Organic Crystals. *Microsc Microanal* **2020,** *26*, 786-787.
56. Kuei, B.; Aplan, M. P.; Litofsky, J. H.; Gomez, E. D., New opportunities in transmission electron microscopy of polymers. *Mat Sci Eng R* **2020,** *139*.
57. Andrews, E. H.; Gee, G., Crystalline morphology in thin films of natural rubber II. Crystallization under strain. *Proceedings of the Royal Society of London. Series A. Mathematical and Physical Sciences* **1964,** *277*, 562-570.
58. Andrews, E. H.; Stubbs, J. M., A NEW FREEZING HEAD FOR THE ULTRAMICROTOMY OF RUBBERS. *Journal of the Royal Microscopical Society* **1964,** *82*, 221-223.
59. KATO, K., Electron Microscopy of ABS Plastics. *Journal of electron microscopy* **1965,** *14*, 220-221.
60. Kato, K., Osmium Tetroxide Fixation of Rubber Latices. *Journal of electron microscopy* **1965,** 1*4*, 219-220.
61. Swartzendruber, D. C.; Burnett, I. H.; Wertz, P. W.; Madison, K. C.; Squier, C. A., Osmium-Tetroxide and Ruthenium Tetroxide Are Complementary Reagents for the Preparation of Epidermal Samples for Transmission Electron-Microscopy. *J Invest Dermatol* **1995,** *104*, 417-420.
62. Ruokolainen, J.; Tanner, J.; Ikkala, O.; ten Brinke, G.; Thomas, E. L., Direct imaging of self-organized Comb copolymer-like systems obtained by hydrogen bonding: Poly(4-vinylpyridine)-4-nonadecylphenol. *Macromolecules* **1998,** *31*, 3532-3536.
63. Boyde, A.; Mccorkell, F. A.; Taylor, G. K.; Bomphrey, R. J.; Doube, M., Iodine Vapor Staining for Atomic Number Contrast in Backscattered Electron and X-Ray Imaging. *Microsc Res Techniq* **2014,** *77*, 1044-1051.
64. Hayat, M. A., 4 - Positive Staining. In *Basic Techniques for Transmission Electron Microscopy*, Hayat, M. A., Ed. Academic Press: **1986,** 182-231.
65. Mineart, K. P.; Jiang, X.; Jinnai, H.; Takahara, A.; Spontak, R. J., Morphological Investigation of Midblock-Sulfonated Block Ionomers Prepared from Solvents Differing in Polarity. *Macromolecular rapid communications* **2015,** *36*, 432-438.
66. Michler, G. H.; Naumann, I., Elektronenmikroskopische Untersuchungen von Polyethylenen. III. Bestimmung der Lamellendicken. *Acta Polymerica* **1982,** *33*, 399-407.
67. Haubruge, H. G.; Jonas, A. M.; Legras, R., Staining of poly(ethylene terephthalate) by ruthenium tetroxide. *Polymer* **2003,** *44*, 3229-3234.

68. Michler, G. H., Contrast Enhancement. In *Electron Microscopy of Polymers*, Michler, G. H., Ed. Springer Berlin Heidelberg: Berlin, Heidelberg, **2008,** 241-260.
69. Yakovlev, S.; Fiscus, D.; Brant, P.; Butler, J.; Bucknall, D. G.; Downing, K. H., Mechanism of stress induced crystallization of polyethylene. *Polymer* **2019,** *175*, 25-31.
70. Loo, Y. L.; Register, R. A.; Adamson, D. H., Direct imaging of polyethylene crystallites within block copolymer microdomains. *J Polym Sci Pol Phys* **2000,** *38*, 2564-2570.
71. Franken, L. E.; Boekema, E. J.; Stuart, M. C. A., Transmission Electron Microscopy as a Tool for the Characterization of Soft Materials: Application and Interpretation. *Adv Sci* **2017,** *4*, 1600476.
72. Friedrich, H.; Frederik, P. M.; de With, G.; Sommerdijk, N. A. J. M., Imaging of Self-Assembled Structures: Interpretation of TEM and Cryo-TEM Images. *Angew Chem Int Edit* **2010,** *49*, 7850-7858.
73. Trent, J. S., Ruthenium Tetraoxide Staining of Polymers - New Preparative Methods for Electron-Microscopy. *Macromolecules* **1984,** *17*, 2930-2931.
74. Melchior, V.; Hollingshead, C. J.; Cahoon, M. E., Stacking in Lipid Vesicle Tubulin Mixtures Is an Artifact of Negative Staining. *J Cell Biol* **1980,** *86*, 881-884.
75. De Carlo, S.; Harris, J. R., Negative staining and cryo-negative staining of macromolecules and viruses for TEM. *Micron* **2011,** *42*, 117-131.
76. Method of the Year 2015. *Nat Methods* **2016,** *13*, 1-1.
77. Eisenstein, M., The field that came in from the cold. *Nat Methods* **2016,** *13*, 19-22.
78. Glaeser, R. M., How good can cryo-EM become? *Nat Methods* **2016,** *13*, 28-32.
79. Cheng, Y. F., Single-Particle Cryo-EM at Crystallographic Resolution. *Cell* **2015,** *161*, 450-457.
80. Scheres, S. H. W., Processing of Structurally Heterogeneous Cryo-EM Data in RELION. *Resolution Revolution: Recent Advances in Cryoem* **2016,** *579*, 125-157.
81. Milazzo, A. C.; Cheng, A.; Moeller, A.; Lyumkis, D.; Jacovetty, E.; Polukas, J.; Ellisman, M. H.; Xuong, N. H.; Carragher, B.; Potter, C. S., Initial evaluation of a direct detection device detector for single particle cryo-electron microscopy. *Journal of structural biology* **2011,** *176*, 404-8.
82. Bammes, B. E.; Rochat, R. H.; Jakana, J.; Chen, D. H.; Chiu, W., Direct electron detection yields cryo-EM reconstructions at resolutions beyond 3/4 Nyquist frequency. *Journal of structural biology* **2012,** *177*, 589-601.
83. Zheng, S. Q.; Palovcak, E.; Armache, J. P.; Verba, K. A.; Cheng, Y. F.; Agard, D. A., MotionCor2: anisotropic correction of beam-induced motion for improved cryo-electron microscopy. *Nat Methods* **2017,** *14*, 331-332.
84. Rohou, A.; Grigorieff, N., CTFFIND4: Fast and accurate defocus estimation from electron micrographs. *Journal of structural biology* **2015,** *192*, 216-21.
85. Zhang, K., Gctf: Real-time CTF determination and correction. *Journal of structural biology* **2016,** *193*, 1-12.
86. Williams, D. B.; Carter, C. B., Phase-Contrast Images. In *Transmission Electron Microscopy: A Textbook for Materials Science*, Williams, D. B.; Carter, C. B., Eds. Springer US: Boston, MA, 2009.

87. Danev, R.; Buijsse, B.; Khoshouei, M.; Plitzko, J. M.; Baumeister, W., Volta potential phase plate for in-focus phase contrast transmission electron microscopy. *Proc Natl Acad Sci U S A* **2014,** *111*, 15635-40.
88. Tosaka, M.; Danev, R.; Nagayama, K., Application of phase contrast transmission microscopic methods to polymer materials. *Macromolecules* **2005,** *38*, 7884-7886.
89. Fukuda, Y.; Laugks, U.; Lucic, V.; Baumeister, W.; Danev, R., Electron cryotomography of vitrified cells with a Volta phase plate. *Journal of structural biology* **2015,** *190*, 143-154.
90. Danev, R.; Baumeister, W., Cryo-EM single particle analysis with the Volta phase plate. *Elife* **2016,** *5*, e13046.
91. Danev, R.; Tegunov, D.; Baumeister, W., Using the Volta phase plate with defocus for cryo-EM single particle analysis. *Elife* **2017,** *6*, e23006.
92. Fan, X.; Zhao, L. Y.; Liu, C.; Zhang, J. C.; Fan, K. L.; Yan, X. Y.; Peng, H. L.; Lei, J. L.; Wang, H. W., Near-Atomic Resolution Structure Determination in Over-Focus with Volta Phase Plate by Cs-Corrected Cryo-EM. *Structure* **2017,** *25*, 1623-1630.
93. Khoshouei, M.; Radjainia, M.; Baumeister, W.; Danev, R., Cryo-EM structure of haemoglobin at 3.2 angstrom determined with the Volta phase plate. *Nat Commun* **2017,** *8*.
94. Pretzsch, R.; Dries, M.; Hettler, S.; Spiecker, M.; Obermair, M.; Gerthsen, D., Investigation of hole-free phase plate performance in transmission electron microscopy under different operation conditions by experiments and simulations. *Adv Struct Chem Imag* **2019,** *5*, 5.
95. Schwartz, O.; Axelrod, J. J.; Glaeser, R. M.; Muller, H., Laser-Based Zernike Plate for Phase Contrast Transmission Electron Microscopy. *Biophys J* **2018,** *114*, 160a-160a.
96. Schwartz, O.; Axelrod, J. J.; Campbell, S. L.; Turnbaugh, C.; Glaeser, R. M.; Muller, H., Laser phase plate for transmission electron microscopy. *Nat Methods* **2019,** *16*, 1016-1020.
97. Shefelbine, T. A.; Vigild, M. E.; Matsen, M. W.; Hajduk, D. A.; Hillmyer, M. A.; Cussler, E. L.; Bates, F. S., Core-shell gyroid morphology in a poly(isoprene-block-styrene-block-dimethylsiloxane) triblock copolymer. *J Am Chem Soc* **1999,** *121*, 8457-8465.
98. Mareau, V. H.; Akasaka, S.; Osaka, T.; Hasegawa, H., Direct visualization of the perforated layer/gyroid grain boundary in a polystyrene-block-polyisoprene/polystyrene blend by electron tomography. *Macromolecules* **2007,** *40*, 9032-9039.
99. Spontak, R. J.; Williams, M. C.; Agard, D. A., Three-dimensional study of cylindrical morphology in a styrene-butadiene-styrene block copolymer. *Polymer* **1988,** *29*, 387-395.
100. Frank, J., *Electron Tomography: Methods for Three-Dimensional Visualization of Structures in the Cell*. 2nd Edition ed.; Springer, Albany, NY: 2006.
101. Kak, A. C.; Slaney, M., *Principles of Computerized Tomographic Imaging*. Society for Industrial and Applied Mathematics: 2001.
102. Jinnai, H.; Spontak, R. J.; Nishi, T., Transmission Electron Microtomography and Polymer Nanostructures. *Macromolecules* **2010,** *43*, 1675-1688.
103. Nudelman, F.; de With, G.; Sommerdijk, N. A. J. M., Cryo-electron tomography: 3-dimensional imaging of soft matter. *Soft Matter* **2011,** *7*, 17-24.
104. Patterson, J. P.; Xu, Y. F.; Moradi, M. A.; Sommerdijk, N. A. J. M.; Friedrich, H., CryoTEM as an Advanced Analytical Tool for Materials Chemists. *Accounts Chem Res* **2017,** *50*, 1495-1501.
105. Bals, S.; Van Aert, S.; Van Tendeloo, G., High resolution electron tomography. *Curr Opin Solid St M* **2013,** *17*, 107-114.

106. Midgley, P. A.; Weyland, M., 3D electron microscopy in the physical sciences: the development of Z-contrast and EFTEM tomography. *Ultramicroscopy* **2003,** *96*, 413-431.
107. Henderson, R.; Unwin, P. N., Three-dimensional model of purple membrane obtained by electron microscopy. *Nature* **1975,** *257*, 28-32.
108. De Rosier, D. J.; Klug, A., Reconstruction of Three Dimensional Structures from Electron Micrographs. *Nature* **1968,** *217*, 130-134.
109. Amos, L. A.; Henderson, R.; Unwin, P. N., Three-dimensional structure determination by electron microscopy of two-dimensional crystals. *Prog Biophys Mol Biol* **1982,** *39*, 183-231.
110. Walz, T.; Grigorieff, N., Electron crystallography of two-dimensional crystals of membrane proteins. *Journal of structural biology* **1998,** *121*, 142-161.
111. Downing, K. H.; Nogales, E., Cryoelectron Microscopy Applications in the Study of Tubulin Structure, Microtubule Architecture, Dynamics and Assemblies, and Interaction of Microtubules with Motors. *Methods in Enzymology, Vol 483: Cryo-Em, Part C: Analyses, Interpretation, and Case Studies* **2010,** *483*, 121-142.
112. Frank, J., *Three-dimensional electron microscopy of macromolecular assemblies : visualization of biological molecules in their native state*. 2nd ed.; Oxford University Press: New York, 2006.
113. Scheres, S. H., A Bayesian view on cryo-EM structure determination. *J Mol Biol* **2012,** *415*, 406-18.
114. Bai, X. C.; McMullan, G.; Scheres, S. H. W., How cryo-EM is revolutionizing structural biology. *Trends Biochem Sci* **2015,** *40*, 49-57.
115. Cheng, Y.; Grigorieff, N.; Penczek, P. A.; Walz, T., A Primer to Single-Particle Cryo-Electron Microscopy. *Cell* **2015,** *161*, 438-449.
116. Lafleur, R. P. M.; Herziger, S.; Schoenmakers, S. M. C.; Keizer, A. D. A.; Jahzerah, J.; Thota, B. N. S.; Su, L.; Bomans, P. H. H.; Sommerdijk, N. A. J. M.; Palmans, A. R. A.; Haag, R.; Friedrich, H.; Bottcher, C.; Meijer, E. W., Supramolecular Double Helices from Small C-3-Symmetrical Molecules Aggregated in Water. *J Am Chem Soc* **2020,** *142*, 17644-17652.
117. Sui, H. X.; Downing, K. H., Molecular architecture of axonemal microtubule doublets revealed by cryo-electron tomography. *Nature* **2006,** *442*, 475-478.
118. Bharat, T. A. M.; Russo, C. J.; Lowe, J.; Passmore, L. A.; Scheres, S. H. W., Advances in Single-Particle Electron Cryomicroscopy Structure Determination applied to Sub-tomogram Averaging. *Structure* **2015,** *23*, 1743-1753.
119. Zhang, P. J., Advances in cryo-electron tomography and subtomogram averaging and classification. *Curr Opin Struc Biol* **2019,** *58*, 249-258.
120. Talmon, Y.; Davis, H. T.; Scriven, L. E.; Thomas, E. L., Cold-Stage Microscopy System for Fast-Frozen Liquids. *Rev Sci Instrum* **1979,** *50*, 698-704.
121. Wolf, L.; Hoffmann, H.; Talmon, Y.; Teshigawara, T.; Watanabe, K., Cryo-TEM imaging of a novel microemulsion system of silicone oil with an anionic/nonionic surfactant mixture. *Soft Matter* **2010,** *6*, 5367-5374.
122. Cui, H.; Hodgdon, T. K.; Kaler, E. W.; Abezgauz, L.; Danino, D.; Lubovsky, M.; Talmon, Y.; Pochan, D. J., Elucidating the assembled structure of amphiphiles in solution via cryogenic transmission electron microscopy. *Soft Matter* **2007,** *3*, 945-955.

123. Bang, J.; Jain, S. M.; Li, Z. B.; Lodge, T. P.; Pedersen, J. S.; Kesselman, E.; Talmon, Y., Sphere, cylinder, and vesicle nanoaggregates in poly (styrene-b-isoprene) diblock copolymer solutions. *Macromolecules* **2006,** *39*, 1199-1208.
124. Kesselman, E.; Talmon, Y.; Bang, J.; Abbas, S.; Li, Z. B.; Lodge, T. P., Cryogenic transmission electron microscopy imaging of vesicles formed by a polystyrene-polyisoprene diblock copolymer. *Macromolecules* **2005,** *38*, 6779-6781.
125. Won, Y. Y.; Brannan, A. K.; Davis, H. T.; Bates, F. S., Cryogenic transmission electron microscopy (cryo-TEM) of micelles and vesicles formed in water by polyethylene oxide)-based block copolymers. *J Phys Chem B* **2002,** *106*, 3354-3364.
126. Discher, B. M.; Won, Y. Y.; Ege, D. S.; Lee, J. C. M.; Bates, F. S.; Discher, D. E.; Hammer, D. A., Polymersomes: Tough vesicles made from diblock copolymers. *Science* **1999,** *284*, 1143-1146.
127. Wittemann, A.; Drechsler, M.; Talmon, Y.; Ballauff, M., High elongation of polyelectrolyte chains in the osmotic limit of spherical polyelectrolyte brushes: A study by cryogenic transmission electron microscopy. *J Am Chem Soc* **2005,** *127*, 9688-9689.
128. Bellare, J. R.; Davis, H. T.; Scriven, L. E.; Talmon, Y., Controlled Environment Vitrification System - an Improved Sample Preparation Technique. *J Electron Micr Tech* **1988,** *10*, 87-111.
129. Talmon, Y.; Adrian, M.; Dubochet, J., Electron-Beam Radiation-Damage to Organic Inclusions in Vitreous, Cubic, and Hexagonal Ice. *Journal of microscopy* **1986,** *141*, 375-384.
130. Talmon, Y.; Narkis, M.; Silverstein, M., Electron-Beam Radiation-Damage to Organic Inclusions in Ice as an Analytical Tool for Polymer Science. *J Electron Micr Tech* **1985,** *2*, 589-596.
131. Talmon, Y.; Evans, D. F.; Ninham, B. W., Spontaneous Vesicles Formed from Hydroxide Surfactants - Evidence from Electron-Microscopy. *Science* **1983,** *221*, 1047-1048.
132. Frank, J., Time-resolved cryo-electron microscopy: Recent progress. *Journal of structural biology* **2017,** *200*, 303-306.
133. Dandey, V. P.; Budell, W. C.; Wei, H.; Bobe, D.; Maruthi, K.; Kopylov, M.; Eng, E. T.; Kahn, P. A.; Hinshaw, J. E.; Kundu, N.; Nimigean, C. M.; Fan, C.; Sukomon, N.; Darst, S. A.; Saecker, R. M.; Chen, J.; Malone, B.; Potter, C. S.; Carragher, B., Time-resolved cryo-EM using Spotiton. *Nat Methods* **2020,** *17*, 897-900.
134. Ross, F. M., Opportunities and challenges in liquid cell electron microscopy. *Science* **2015,** *350*, aaa9886.
135. Wu, H. L.; Friedrich, H.; Patterson, J. P.; Sommerdijk, N. A. J. M.; de Jonge, N., Liquid-Phase Electron Microscopy for Soft Matter Science and Biology. *Adv Mater* **2020,** *32*, 2001582.
136. Cho, H.; Jones, M. R.; Nguyen, S. C.; Hauwiller, M. R.; Zettl, A.; Alivisatos, A. P., The Use of Graphene and Its Derivatives for Liquid-Phase Transmission Electron Microscopy of Radiation-Sensitive Specimens. *Nano Lett* **2017,** *17*, 414-420.
137. Park, J.; Koo, K.; Noh, N.; Chang, J. H.; Cheong, J. Y.; Dae, K. S.; Park, J. S.; Ji, S.; Kim, I.-D.; Yuk, J. M., Graphene Liquid Cell Electron Microscopy: Progress, Applications, and Perspectives. *ACS nano* **2021,** *15*, 288-308.
138. Ianiro, A.; Wu, H. L.; van Rijt, M. M. J.; Vena, M. P.; Keizer, A. D. A.; Esteves, A. C. C.; Tuinier, R.; Friedrich, H.; Sommerdijk, N. A. J. M.; Patterson, J. P., Liquid-liquid phase separation during amphiphilic self-assembly. *Nat Chem* **2019,** *11*, 320-328.

139. Blanazs, A.; Armes, S. P.; Ryan, A. J., Self-Assembled Block Copolymer Aggregates: From Micelles to Vesicles and their Biological Applications. *Macromolecular rapid communications* **2009,** *30*, 267-277.
140. Tritschler, U.; Pearce, S.; Gwyther, J.; Whittell, G. R.; Manners, I., 50th Anniversary Perspective: Functional Nanoparticles from the Solution Self-Assembly of Block Copolymers. *Macromolecules* **2017,** *50*, 3439-3463.
141. Zhang, W. Y.; Kochovski, Z.; Lu, Y.; Schmidt, B. V. K. J.; Antonietti, M.; Yuan, J. Y., Internal Morphology-Controllable Self-Assembly in Poly(Ionic Liquid) Nanoparticles. *ACS nano* **2016,** *10*, 7731-7737.
142. Drummy, L. F.; Davis, R. J.; Moore, D. L.; Durstock, M.; Vaia, R. A.; Hsu, J. W. P., Molecular-Scale and Nanoscale Morphology of P3HT:PCBM Bulk Heterojunctions: Energy-Filtered TEM and Low-Dose HREM. *Chemistry of Materials* **2011,** *23*, 907-912.
143. Vakhshouri, K.; Kozub, D. R.; Wang, C. C.; Salleo, A.; Gomez, E. D., Effect of Miscibility and Percolation on Electron Transport in Amorphous Poly(3-Hexylthiophene)/Phenyl-C-61-Butyric Acid Methyl Ester Blends. *Phys Rev Lett* **2012,** *108*.
144. Wirix, M. J. M.; Bomans, P. H. H.; Friedrich, H.; Sommerdijk, N. A. J. M.; de With, G., Three-Dimensional Structure of P3HT Assemblies in Organic Solvents Revealed by Cryo-TEM. *Nano Lett* **2014,** *14*, 2033-2038.
145. Tahara, Y.; Fujiyoshi, Y., A New Method to Measure Bilayer Thickness - Cryoelectron Microscopy of Frozen-Hydrated Liposomes and Image Simulation. *Micron* **1994,** *25*, 141-149.
146. Wang, L. G.; Bose, P. S.; Sigworth, F. J., Using cryo-EM to measure the dipole potential of a lipid membrane. *P Natl Acad Sci USA* **2006,** *103*, 18528-18533.
147. Bermudez, H.; Hammer, D. A.; Discher, D. E., Effect of bilayer thickness on membrane bending rigidity. *Langmuir* **2004,** *20*, 540-543.
148. Sun, J.; Zuckermann, R. N., Peptoid Polymers: A Highly Designable Bioinspired Material. *ACS nano* **2013,** *7*, 4715-4732.
149. Jiang, X.; Spencer, R. K.; Sun, J.; Ophus, C.; Zuckermann, R. N.; Downing, K. H.; Balsara, N. P., Resolving the Morphology of Peptoid Vesicles at the 1 nm Length Scale Using Cryogenic Electron Microscopy. *J Phys Chem B* **2019,** *123*, 1195-1205.
150. Cornell, C. E.; Mileant, A.; Thakkar, N.; Lee, K. K.; Keller, S. L., Direct imaging of liquid domains in membranes by cryo-electron tomography. *P Natl Acad Sci USA* **2020,** *117*, 19713-19719.
151. Messmer, D.; Bottcher, C.; Yu, H.; Halperin, A.; Binder, K.; Kroger, M.; Schlutert, A. D., 3D Conformations of Thick Synthetic Polymer Chains Observed by Cryogenic Electron Microscopy. *ACS nano* **2019,** *13*, 3466-3473.
152. Farha, O. K.; Eryazici, I.; Jeong, N. C.; Hauser, B. G.; Wilmer, C. E.; Sarjeant, A. A.; Snurr, R. Q.; Nguyen, S. T.; Yazaydin, A. O.; Hupp, J. T., Metal-Organic Framework Materials with Ultrahigh Surface Areas: Is the Sky the Limit? *J Am Chem Soc* **2012,** *134*, 15016-15021.
153. Zhou, H. C.; Long, J. R.; Yaghi, O. M., Introduction to Metal-Organic Frameworks. *Chem Rev* **2012,** *112*, 673-674.
154. Goetjen, T. A.; Liu, J.; Wu, Y. F.; Sui, J. Y.; Zhang, X.; Hupp, J. T.; Farha, O. K., Metal-organic framework (MOF) materials as polymerization catalysts: a review and recent advances. *Chem Commun* **2020,** *56*, 10409-10418.

155. Wang, H. L.; He, S. F.; Qin, X. D.; Li, C. E.; Li, T., Interfacial Engineering in Metal-Organic Framework-Based Mixed Matrix Membranes Using Covalently Grafted Polyimide Brushes. *J Am Chem Soc* **2018,** *140*, 17203-17210.
156. Kalaj, M.; Bentz, K. C.; Ayala, S.; Palomba, J. M.; Barcus, K. S.; Katayama, Y.; Cohen, S. M., MOF-Polymer Hybrid Materials: From Simple Composites to Tailored Architectures. *Chem Rev* **2020,** *120*, 8267-8302.
157. Gu, Y. W.; Huang, M. J.; Zhang, W. X.; Pearson, M. A.; Johnson, J. A., PolyMOF Nanoparticles: Dual Roles of a Multivalent polyMOF Ligand in Size Control and Surface Functionalization. *Angew Chem Int Edit* **2019,** *58*, 16676-16681.
158. MacLeod, M. J.; Johnson, J. A., Block co-polyMOFs: assembly of polymer-polyMOF hybrids via iterative exponential growth and "click" chemistry. *Polym Chem-Uk* **2017,** *8*, 4488-4493.
159. Wang, Y. F.; Zhong, M. J.; Park, J. V.; Zhukhovitskiy, A. V.; Shi, W. C.; Johnson, J. A., Block Co-PolyMOCs by Stepwise Self-Assembly. *J Am Chem Soc* **2016,** *138*, 10708-10715.
160. Wang, Q.; Astruc, D., State of the Art and Prospects in Metal-Organic Framework (MOF)-Based and MOF-Derived Nanocatalysis. *Chem Rev* **2020,** *120*, 1438-1511.
161. Banihashemi, F.; Bu, G.; Thaker, A.; Williams, D.; Lin, J. Y. S.; Nannenga, B. L., Beam-sensitive metal-organic framework structure determination by microcrystal electron diffraction. *Ultramicroscopy* **2020,** *216*, 113048.
162. Patterson, J. P.; Abellan, P.; Denny, M. S.; Park, C.; Browning, N. D.; Cohen, S. M.; Evans, J. E.; Gianneschi, N. C., Observing the Growth of Metal-Organic Frameworks by in Situ Liquid Cell Transmission Electron Microscopy. *J Am Chem Soc* **2015,** *137*, 7322-7328.
163. Ogata, A. F.; Rakowski, A. M.; Carpenter, B. P.; Fishman, D. A.; Merham, J. G.; Hurst, P. J.; Patterson, J. P., Direct Observation of Amorphous Precursor Phases in the Nucleation of Protein-Metal-Organic Frameworks. *J Am Chem Soc* **2020,** *142*, 1433-1442.
164. Zhu, Y. H.; Ciston, J.; Zheng, B.; Miao, X. H.; Czarnik, C.; Pan, Y. C.; Sougrat, R.; Lai, Z. P.; Hsiung, C. E.; Yao, K. X.; Pinnau, I.; Pan, M.; Han, Y., Unravelling surface and interfacial structures of a metal-organic framework by transmission electron microscopy. *Nat Mater* **2017,** *16*, 532-536.
165. Zhang, D. L.; Zhu, Y. H.; Liu, L. M.; Ying, X. R.; Hsiung, C. E.; Sougrat, R.; Li, K.; Han, Y., Atomic-resolution transmission electron microscopy of electron beam-sensitive crystalline materials. *Science* **2018,** *359*, 675-679.
166. Li, Y. Z.; Wang, K. C.; Zhou, W. J.; Li, Y. B.; Vila, R.; Huang, W.; Wang, H. X.; Chen, G. X.; Wu, G. H.; Tsao, Y. C.; Wang, H. S.; Sinclair, R.; Chiu, W.; Cui, Y., Cryo-EM Structures of Atomic Surfaces and Host-Guest Chemistry in Metal-Organic Frameworks (vol 1, pg 428, 2019). *Matter* **2020,** *2*, 1064-1064.
167. Nam, K. T.; Shelby, S. A.; Choi, P. H.; Marciel, A. B.; Chen, R.; Tan, L.; Chu, T. K.; Mesch, R. A.; Lee, B. C.; Connolly, M. D.; Kisielowski, C.; Zuckermann, R. N., Free-floating ultrathin two-dimensional crystals from sequence-specific peptoid polymers. *Nat Mater* **2010,** *9*, 454-460.
168. Xuan, S. T.; Jiang, X.; Spencer, R. K.; Li, N. K.; Prendergast, D.; Balsara, N. P.; Zuckermann, R. N., Atomic-level engineering and imaging of polypeptoid crystal lattices. *P Natl Acad Sci USA* **2019,** *116*, 22491-22499.

169. Jiang, X.; Xuan, S. T.; Kundu, J.; Prendergast, D.; Zuckermann, R. N.; Balsara, N. P., Effect of processing and end groups on the crystal structure of polypeptoids studied by cryogenic electron microscopy at atomic length scales. *Soft Matter* **2019,** *15*, 4723-4736.
170. Jiang, X.; Greer, D. R.; Kundu, J.; Ophus, C.; Minor, A. M.; Prendergast, D.; Zuckermann, R. N.; Balsara, N. P.; Downing, K. H., Imaging Unstained Synthetic Polymer Crystals and Defects on Atomic Length Scales Using Cryogenic Electron Microscopy. *Macromolecules* **2018,** *51*, 7794-7799.
171. Pradere, P.; Thomas, E. L., Antiphase Boundaries and Ordering Defects in Syndiotactic Polystyrene Crystals. *Macromolecules* **1990,** *23*, 4954-4958.
172. Pennycook, S. J. N., P.D., *Scanning Transmission Electron Microscopy Imaging and Analysis*. Springer, New York, NY: 2011.
173. Benetatos, N. M.; Smith, B. W.; Heiney, P. A.; Winey, K. I., Toward Reconciling STEM and SAXS Data from Ionomers by Investigating Gold Nanoparticles. *Macromolecules* **2005,** *38*, 9251-9257.
174. Zhou, N. C.; Chan, C. D.; Winey, K. I., Reconciling STEM and X-ray scattering data to determine the nanoscale ionic aggregate morphology in sulfonated polystyrene ionomers. *Macromolecules* **2008,** *41*, 6134-6140.
175. Loos, J.; Sourty, E.; Lu, K. B.; de With, G.; van Bavel, S., Imaging Polymer Systems with High-Angle Annular Dark Field Scanning Transmission Electron Microscopy (HAADF-STEM). *Macromolecules* **2009,** *42*, 2581-2586.
176. Yakovlev, S.; Wang, X.; Ercius, P.; Balsara, N. P.; Downing, K. H., Direct Imaging of Nanoscale Acidic Clusters in a Polymer Electrolyte Membrane. *J Am Chem Soc* **2011,** *133*, 20700-20703.
177. Aso, R.; Kurata, H.; Namikoshi, T.; Hashimoto, T.; Kuo, S.-W.; Chang, F.-C.; Hasegawa, H.; Tsujimoto, M.; Takano, M.; Isoda, S., Quantitative Imaging of Tg in Block Copolymers by Low-Angle Annular Dark-Field Scanning Transmission Electron Microscopy. *Macromolecules* **2013,** *46*, 8589-8595.
178. Yakovlev, S.; Downing, K. H., Visualization of clusters in polymer electrolyte membranes by electron microscopy. *Phys Chem Chem Phys* **2013,** *15*, 1052-1064.
179. Jinnai, H.; Higuchi, T.; Zhuge, X. D.; Kumamoto, A.; Batenburg, K. J.; Ikuhara, Y., Three-Dimensional Visualization and Characterization of Polymeric Self-Assemblies by Transmission Electron Microtomography. *Accounts Chem Res* **2017,** *50*, 1293-1302.
180. Takacs, C. J.; Treat, N. D.; Kramer, S.; Chen, Z. H.; Facchetti, A.; Chabinyc, M. L.; Heeger, A. J., Remarkable Order of a High-Performance Polymer. *Nano Lett* **2013,** *13*, 2522-2527.
181. Leijten, Z. J. W. A.; Wirix, M. J. M.; Lazar, S.; Verhoeven, W.; Luiten, O. J.; de With, G.; Friedrich, H., Nanoscale chemical analysis of beam-sensitive polymeric materials by cryogenic electron microscopy. *J Polym Sci* **2021**. 1-11.
182. Glaeser, R. M., Invited Review Article: Methods for imaging weak-phase objects in electron microscopy. *Rev Sci Instrum* **2013,** *84*, 111101.
183. Ophus, C.; Ercius, P.; Huijben, M.; Ciston, J., Non-spectroscopic composition measurements of SrTiO3-La0.7Sr0.3MnO3 multilayers using scanning convergent beam electron diffraction. *Appl Phys Lett* **2017,** *110*, 063102.

184. Gammer, C.; Ozdol, V. B.; Liebscher, C. H.; Minor, A. M., Diffraction contrast imaging using virtual apertures. *Ultramicroscopy* **2015,** *155*, 1-10.
185. Ozdol, V. B.; Gammer, C.; Jin, X. G.; Ercius, P.; Ophus, C.; Ciston, J.; Minor, A. M., Strain mapping at nanometer resolution using advanced nano-beam electron diffraction. *Appl Phys Lett* **2015,** *106*, 253107.
186. Nellist, P. D.; Mccallum, B. C.; Rodenburg, J. M., Resolution Beyond the Information Limit in Transmission Electron-Microscopy. *Nature* **1995,** *374*, 630-632.
187. Panova, O.; Chen, X. C.; Bustillo, K. C.; Ophus, C.; Bhatt, M. P.; Balsara, N.; Minor, A. M., Orientation mapping of semicrystalline polymers using scanning electron nanobeam diffraction. *Micron* **2016,** *88*, 30-36.
188. Panova, O.; Ophus, C.; Takacs, C. J.; Bustillo, K. C.; Balhorn, L.; Salleo, A.; Balsara, N.; Minor, A. M., Diffraction imaging of nanocrystalline structures in organic semiconductor molecular thin films. *Nat Mater* **2019,** *18*, 860-865.
189. Gallagher-Jones, M.; Ophus, C.; Bustillo, K. C.; Boyer, D. R.; Panova, O.; Glynn, C.; Zee, C. T.; Ciston, J.; Mancia, K. C.; Minor, A. M.; Rodriguez, J. A., Nanoscale mosaicity revealed in peptide microcrystals by scanning electron nanodiffraction. *Communications Biology* **2019,** *2*, 26.
190. Ophus, C., Four-Dimensional Scanning Transmission Electron Microscopy (4D-STEM): From Scanning Nanodiffraction to Ptychography and Beyond. *Microsc Microanal* **2019,** *25*, 563-582.
191. Savitzky, B. H.; Hughes, L. A.; Zeltmann, S. E.; Brown, H. G.; Zhao, S.; Pelz, P. M.; Barnard, E. S.; Donohue, J.; Rangel DaCosta, L.; Pekin, T. C.; Kennedy, E.; Janish, M. T.; Schneider, M. M.; Herring, P.; Gopal, C.; Anapolsky, A.; Ercius, P.; Scott, M.; Ciston, J.; Minor, A. M.; Ophus, C., py4DSTEM: a software package for multimodal analysis of four-dimensional scanning transmission electron microscopy datasets. *arXiv e-prints* **2020**, arXiv:2003.09523.
192. de Graaf, S.; Momand, J.; Mitterbauer, C.; Lazar, S.; Kooi, B. J., Resolving hydrogen atoms at metal-metal hydride interfaces. *Science Advances* **2020,** *6*, eaay4312.
193. Lazic, I.; Bosch, E. G. T.; Lazar, S., Phase contrast STEM for thin samples: Integrated differential phase contrast. *Ultramicroscopy* **2016,** *160*, 265-280.
194. Lubk, A.; Zweck, J., Differential phase contrast: An integral perspective. *Phys Rev A* **2015,** *91*, 023805
195. Inamoto, S.; Shimomura, S.; Otsuka, Y., Electrostatic potential imaging of phase-separated structures in organic materials via differential phase contrast scanning transmission electron microscopy. *Microscopy-Jpn* **2020,** *69*, 304-311.
196. Inamoto, S.; Yoshida, A.; Otsuka, Y., Three-dimensional Analysis of Non-stained Polymer Alloy Using Differential Phase Contrast-STEM Tomography. *Microsc Microanal* **2019,** *25*, 1826-1827.
197. Shen, B. Y.; Chen, X.; Shen, K.; Xiong, H.; Wei, F., Imaging the node-linker coordination in the bulk and local structures of metal-organic frameworks. *Nat Commun* **2020,** *11*, 2692
198. Li, X. H.; Wang, J. J.; Liu, X.; Liu, L. M.; Cha, D.; Zheng, X. L.; Yousef, A. A.; Song, K. P.; Zhu, Y. H.; Zhang, D. L.; Han, Y., Direct Imaging of Tunable Crystal Surface Structures of MOF MIL-101 Using High-Resolution Electron Microscopy. *J Am Chem Soc* **2019,** *141*, 12021-12028.

199. Ziatdinov, S. V. K. a. O. D. a. S. J. a. M., Machine learning of chemical transformations in the Si-graphene system from atomically resolved images via variational autoencoder. *arXiv* **2020,** *2006.10267*.
200. Maksov, A.; Dyck, O.; Wang, K.; Xiao, K.; Geohegan, D. B.; Sumpter, B. G.; Vasudevan, R. K.; Jesse, S.; Kalinin, S. V.; Ziatdinov, M., Deep learning analysis of defect and phase evolution during electron beam-induced transformations in WS2. *Npj Comput Mater* **2019,** *5*, 12.
201. Palovcak, E.; Asarnow, D.; Campbell, M. G.; Yu, Z. L.; Cheng, Y. F., Enhancing the signal-to-noise ratio and generating contrast for cryo-EM images with convolutional neural networks. *Iucrj* **2020,** *7*, 1142-1150.
202. Zhu, Y. N.; Ouyang, Q.; Mao, Y. D., A deep convolutional neural network approach to single-particle recognition in cryo-electron microscopy. *Bmc Bioinformatics* **2017,** *18*, 384.
203. Matsumoto, S.; Ishida, S.; Araki, M.; Kato, T.; Terayama, K.; Okuno, Y., Extraction of protein dynamics information from cryo-EM maps using deep learning. *Nat Mach Intell* **2021,** *3*, 153-160.
204. Chen, M.; Dai, W.; Sun, S. Y.; Jonasch, D.; He, C. Y.; Schmid, M. F.; Chiu, W.; Ludtke, S. J., Convolutional neural networks for automated annotation of cellular cryo-electron tomograms. *Nat Methods* **2017,** *14*, 983-985.
205. Altantzis, T.; Lobato, I.; De Backer, A.; Beche, A.; Zhang, Y.; Basak, S.; Porcu, M.; Xu, Q.; Sanchez-Iglesias, A.; Liz-Marzan, L. M.; Van Tendeloo, G.; Van Aert, S.; Bals, S., Three-Dimensional Quantification of the Facet Evolution of Pt Nanoparticles in a Variable Gaseous Environment. *Nano Lett* **2019,** *19*, 477-481.
206. Qu, E. Z.; Jimenez, A. M.; Kumar, S. K.; Zhang, K., Quantifying Nanoparticle Assembly States in a Polymer Matrix through Deep Learning. *Macromolecules* **2021,** *54*, 3034-3040.
207. Malac, M.; Hettler, S.; Hayashida, M.; Kano, E.; Egerton, R. F.; Beleggia, M., Phase plates in the transmission electron microscope: operating principles and applications. *Microscopy-Jpn* **2021,** *70*, 75-115.
208. Russo, C. J.; Passmore, L. A., Ultrastable gold substrates for electron cryomicroscopy. *Science* **2014,** *346*, 1377-1380.
209. Chreifi, G.; Chen, S. Y.; Metskas, L. A.; Mastronarde, D.; Jensen, G. J., Cryo-Electron Tomography, Faster: Development of a Fast-Incremental Tilting Scheme for Rapid Tomogram Acquisition. *Biophys J* **2019,** *116*, 575a-575a.
210. Albrecht, W.; Bals, S., Fast Electron Tomography for Nanomaterials. *The Journal of Physical Chemistry C* **2020,** *124*, 27276-27286.
211. Jiang, Y.; Chen, Z.; Hang, Y. M.; Deb, P.; Gao, H.; Xie, S. E.; Purohit, P.; Tate, M. W.; Park, J.; Gruner, S. M.; Elser, V.; Muller, D. A., Electron ptychography of 2D materials to deep sub-angstrom resolution. *Nature* **2018,** *559*, 343-349.

Table of Content

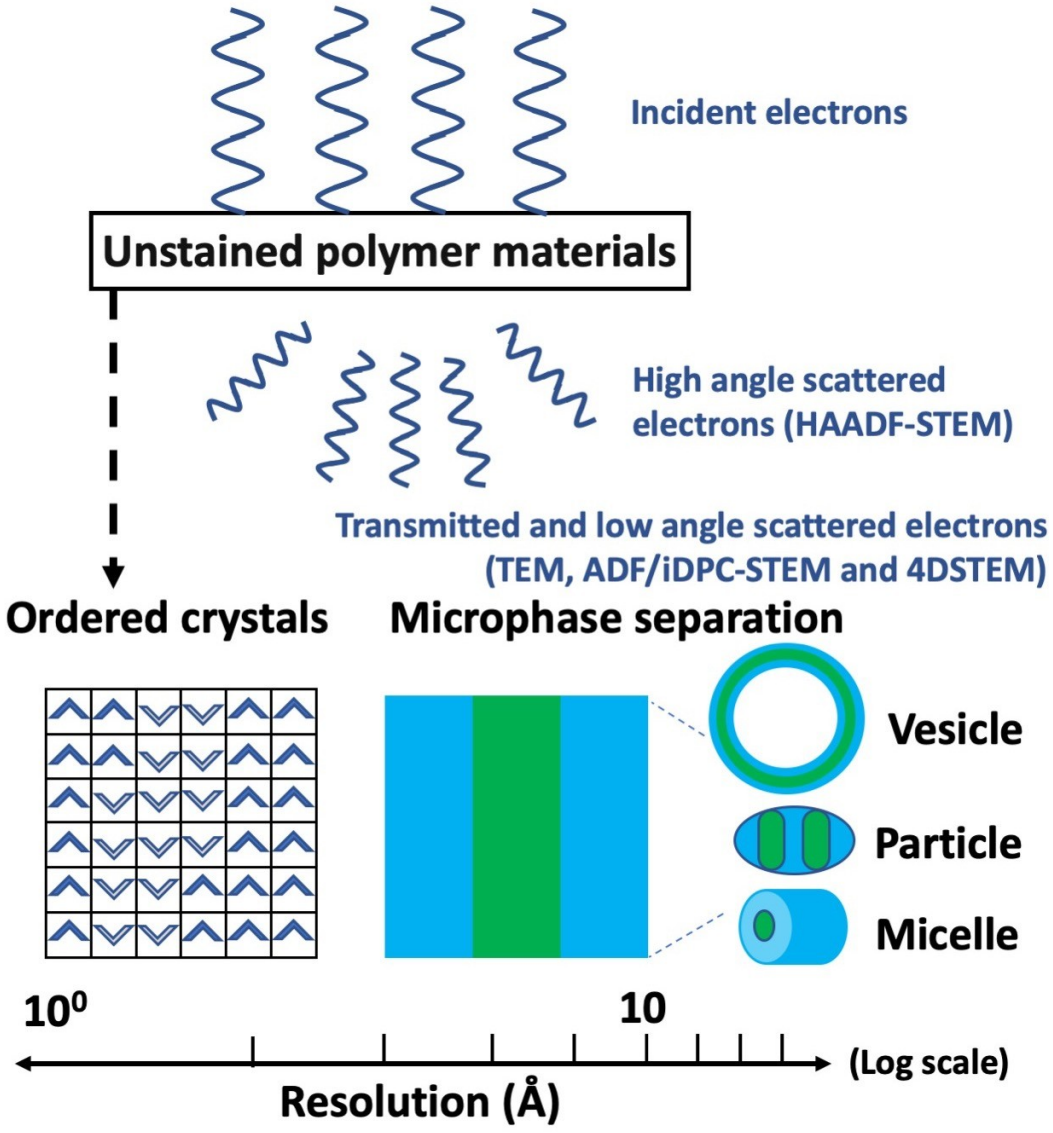
Incident electrons
Unstained polymer materials
High angle scattered
electrons (HAADF-STEM)
Transmitted and low angle scattered electrons
(TEM, ADF/iDPC-STEM and 4DSTEM)
Ordered crystals
Microphase separation
Vesicle
Particle
Micelle
10^0
10
(Log scale)
Resolution (Å)